Exploring Reaction Pathways in Li-ion Batteries with *Operando* Gas Analysis

ROBIN LUNDSTRÖM

Dissertation presented at Uppsala University to be publicly examined in Polhemssalen, Ångströmlaboratoriet, Lägerhyddsvägen 1, Uppsala, Friday, 22 March 2024 at 09:15 for the degree of Doctor of Philosophy. The examination will be conducted in English. Faculty examiner: Dr Isidora Cekic-Laskovic (Helmholtz-Institut Münster).

Abstract

Lundström, R. 2024. Exploring Reaction Pathways in Li-ion Batteries with *Operando* Gas Analysis. *Digital Comprehensive Summaries of Uppsala Dissertations from the Faculty of Science and Technology* 2363. 80 pp. Uppsala: Acta Universitatis Upsaliensis. ISBN 978-91-513-2034-2.

The reliance on Li-ion batteries is increasing as we transition from fossil fuels to renewable energy sources. Despite their widespread use, a gap remains in understanding certain processes within these batteries, especially regarding the solid electrolyte interphase (SEI) and the impact of side reactions on Li-ion batteries. A custom-made Online Electrochemical Mass Spectrometry (OEMS) instrument was designed to explore these aspects. The OEMS instrument was validated through the study of gas-evolving reactions in the classic $LiCoO_2$ | Graphite system. In-depth studies focusing on the reaction pathways of ethylene carbonate, the archetype Li-ion battery electrolyte solvent, identified the specific reaction pathways contributing to SEI formation. Moreover, ethylene carbonate's interaction with residual contaminants like OH^- from H_2O reduction was explored. It was revealed that the integrity of the SEI can be compromised by minor amounts of contaminants, establishing a competitive dynamic at the negative electrode surface between ethylene carbonate and residual contaminants such as H_2O and HF. Additionally, the roles of additives like vinylene carbonate and lithium bis(oxolato) borate in SEI formation were explored. Vinylene carbonate was shown to form a layer on the negative electrode, but also scavenge protons and H_2O, revealing that it is a multi-functional additive. Lithium bis(oxolato) borate on the other hand formed an SEI layer before H_2O reduction, blocking the residual contaminant and ethylene carbonate from reaching the electrode surface. By providing insights into the negative electrode's interphase and SEI formation through a custom-made OEMS instrument, this research underscores the complexity of reaction pathways and the necessity of considering both major and minor, as well as, primary and secondary reactions for a holistic understanding of Li-ion batteries.

Keywords: Online electrochemical mass spectrometry; Li-ion batteries; Solid electrolyte interphase; Reaction pathways;

Robin Lundström, Department of Chemistry - Ångström, Structural Chemistry, Box 538, Uppsala University, SE-751 21 Uppsala, Sweden.

Till min familj

List of papers

This thesis is based on the following papers, which are referred to in the text by their Roman numerals.

I   <u>R. Lundström</u>, E. J. Berg. Design and Validation of an Online Partial and Total Pressure Measurement System for Li-Ion Cells. *Journal of Power Sources* 2021, 405, 229347.
My Contribution: I was part of the planning of the OEMS instrument. I assembled and programmed the complete system. I prepared all materials, performed all experiments and did the data analysis. I wrote the manuscript with input from my supervisor.

II   T. Melin, <u>R. Lundström</u>, E. J. Berg. Revisiting the Ethylene Carbonate - Propylene Carbonate Mystery with Operando Characterization. *Advanced Materials Interfaces* 2021, 2101258.
My Contribution: I was part of the OEMS data analysis and involved in the scientific discussions and manuscript review.

III   <u>R. Lundström</u>, N. Gogoi, T. Melin, E. J. Berg. Unveiling Reaction Pathways of Ethylene Carbonate and Vinylene Carbonate in Li-ion Batteries. *Submitted*.
My Contribution: I conceptualised and planned the study with input from my supervisor. I prepared all the materials and performed and analysed the electrochemistry and OEMS experiments. I wrote the manuscript with input from co-authors.

IV   N. Mozhzhukhina, E. Flores, <u>R. Lundström</u>, V. Nyström, P. G. Kitz, K. Edström, E. J. Berg. Direct Operando Observation of Double Layer Charging and Early Solid Electrolyte Interphase Formation in Li-Ion Battery Electrolytes. *J. Phys. Chem. Lett.* 2020, 11, 4119-4123.
My Contribution: I performed the OEMS experiments and data analysis, and reviewed the manuscript before publication.

V   <u>R. Lundström</u>, N. Gogoi, X. Hou, E. J. Berg. Competing Ethylene Carbonate Reactions on Carbon Electrode in Li-Ion Batteries. *Journal of The Electrochemical Society* 2023, 170, 040516.
My Contribution: I conceptualised and planned the study with input from my supervisor. I prepared all the materials and performed

and analysed the electrochemistry and OEMS experiments. I wrote the manuscript with input from co-authors.

VI   T. Melin, <u>R. Lundström</u>, E. J. Berg. Elucidating the Reduction Mechanism of Lithium bis(oxalato)borate. *Submitted*.
My Contribution: I conceptualised and planned the study together with co-authors. I prepared materials and performed and analysed the OEMS experiments. I was involved in all discussions and reviewed the manuscript throughout the writing process.

Papers not included in this thesis

- N. Gogoi, E. Bowall, <u>R. Lundström</u>, N. Mozhzhukhina, G. Hernández, P. Broqvist, E. J. Berg. Silyl-Functionalized Electrolyte Additives and Their Reactivity Towards Lewis Bases in Li-ion Cells. *Chem. Mater.* 2022, 34, 8, 3831–3838.

- C. Misiewicz, <u>R. Lundström</u>, A. Istaq, M. Lacey, W. Brant, E. J. Berg. Online Electrochemical Mass Spectrometry on Large-Format Li-ion Cells. *Journal of Power Sources* 2023, 554, 232318.

Contents

Abbreviations

ATR	Attenuated total reflectance
API	Application programming interface
C-SEM	Continuous secondary electron multiplier
CV	Cyclic voltammetry
DEC	Diethyl carbonate
DEMS	Differential electrochemical mass spectrometry
DME	1,2-dimethoxyethane
EC	Ethylene carbonate
EG	Ethylene glycol derivatives
EI	Electron ionization
EQCM	Electrochemical quartz crystal microbalance
GC	Glassy carbon
HDPE	High-density polyethylene
LCO	$LiCoO_2$
LEDC	Lithium ethylene dicarbonate
LFP	$LiFePO_4$
LIB	Li-ion battery
LiBOB	Lithium bis(oxalato)borate
LSV	Linear sweep voltammetry
MID	Multiple ion detection
MS	Mass spectrometry/Mass spectrometer
mpe	mass per electron
m/z	Mass/charge
NMR	Nuclear magnetic resonance
OCV	Open circuit voltage
OEMS	Online electrochemical mass spectrometry
PC	Propylene carbonate
PEEK	Polyether ether ketone
PEG	Poly ethylene glycol
S/N	Signal-to-noise
SERS	Surface-enhanced Raman spectroscopy
SOC	State of charge
TMSPa	Tris-(trimethylsilyl)phosphate
VC	Vinylene carbonate

1. Introduction

1.1 The Great Energy Transition

Future history books will surely describe humanity's reliance on energy in the 21st century, and in these books, the first 50 years will be depicted as a transition period. One can imagine a chapter entitled "The Great Energy Transition" in one of these future history books. A chapter which describes our current efforts to phase out fossil-based systems in favour of renewable energies. Multiple reasons for the energy transition will likely be listed, and a few underlying causes for the energy transition will be connected to climate change, the global temperature increase [1] and its possible disastrous consequences [2]. Our future readers will probably scratch their heads if reading Svante Arrhenius' study published already in 1896 about CO_2 released into the atmosphere affecting the ground temperature [3]. Yet, more than a century later, we continued to set records for CO_2 emissions, primarily from fossil-based energy sources [4, 5], while we verbally reached a consensus on the need to avoid rising temperatures.

A sub-chapter entitled "Energy transition inertia" will describe how the whole energy transition happened at a slower-than-desired pace. Several reasons for the inertia will surely be mentioned [6, 7], but one highlighted factor will be the sporadic and unpredictable energy production associated with renewable energy sources, as they are generally weather-dependent. Intermittent renewable energy production will be described as a challenge for the first decades of the 21st century, due to our constant need to access energy. In other words, renewable energy production and energy consumption do not match to the degree we have grown accustomed to when relying on fossil-based energy sources.

The next sub-chapter will hopefully be entitled "Green energy solutions" and contain all the clever solutions we could muster up in this time of need. Here, one of the pillars holding up the renewable energy society is electric storage solutions, which interface energy production and consumption. Several examples will surely be included, and one is battery technology.

In this sub-chapter of a chapter of a future history book is the technology I have dedicated multiple years of work to. Still, "battery technology" is a broad term and what I have focused on is a sliver of what it encompasses, namely studying interphases and decomposition reactions in lithium-ion batteries via *operando* gas analysis. My work is collected in this thesis, which aims to contribute to the cumulative knowledge needed to write the "Green energy solutions" subchapter and make sure that future generations will get to read about it in a bright classroom, not in a dark bunker.

1.2 Lithium-ion batteries

The lithium-ion battery (LIB) was recognised as one of humanity's most important inventions in the last 100 years when John B. Goodenough, M. Stanley Whittingham and Akira Yoshino were awarded the Nobel Prize in Chemistry in 2019 for their work on LIBs [8]. The high volumetric and gravimetric energy density coupled with excellent performance have put LIBs at the centre of the expanding battery market, where LIBs are widely used in portable electronics and electric vehicles.

A schematic representation of a LIB cell is seen in Figure 1.1. A LIB is a rechargeable battery, whose cell function is to move electrons in an external circuit and ions through the electrolyte solution from the positive electrode to the negative electrode during charge and vice versa during discharge[i]. The electron and ion movements are spontaneous during discharge and can power a load as the process is thermodynamically favourable. The electrons and ions are forced from the positive electrode to the negative electrode during charge by applying external power to the battery cell.

The cell energy (W_{cell}) stored in a battery is determined by the integral of the functions of cell voltage, $U_{cell}(t)$, and current, $I(t)$, where t is time. The
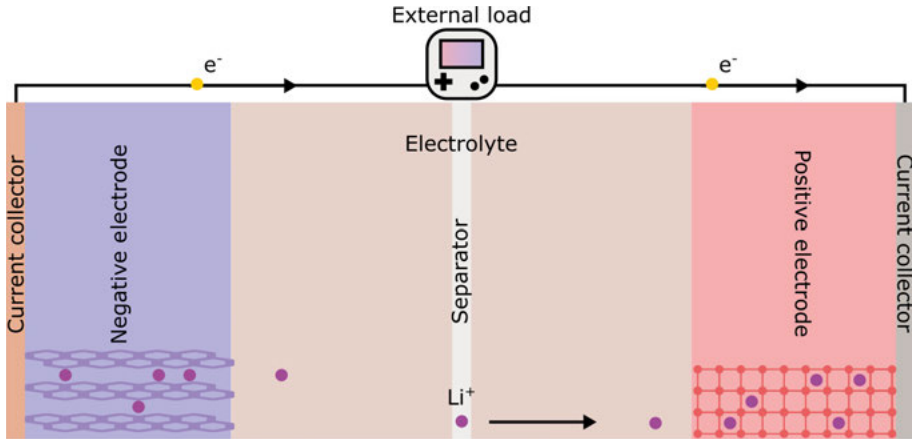
Figure 1.1. Schematic of a LIB during discharge. Li^+ ions travel through the electrolyte solution from the negative to the positive electrode, which are kept from direct contact by a separator. The electrodes are hosts for Li^+ ions when they de-/insert into the electrodes. Electrons travel from the negative electrode to the positive electrode via the current collectors and through an external circuit, powering a load. The arrows indicate the direction for electrons and Li^+ ions during discharge. The direction is reversed during charge.

---

[i]In classical electrochemistry, oxidation and reduction occur at the anode and cathode, respectively. In batteries, on the other hand, the electrode working at a higher potential is normally called the positive electrode during both charging and discharging, and the other electrode is called the negative electrode.

equation is often simplified by multiplying the cell charge capacity (Q_{cell}) and average cell voltage ($U_{average}$):

$$W_{cell} = \int U_{cell}(t)I(t)dt = U_{average}Q_{cell} \qquad (1.1)$$

Increasing both Q_{cell} and U_{cell} results in increased stored energy. However, increasing the capacity and voltage of a battery is not a trivial task, and several caveats are introduced when pushing the energy limit of a battery [9]. In this thesis, the primary focus lies on the necessary considerations for enabling a large U_{cell} (or wide operating voltage window), and a major challenge, unavoidable reductive decomposition of electrolyte, is addressed.

1.2.1 Electrolyte

The base function of an electrolyte is to transport Li^+ ions back and forth between the electrodes at a sufficient rate not to limit the current. Many parameters must be considered for a well-performing electrolyte, such as ionic conductivity, wettability of electrodes and separator, and chemical/thermal stability. However, optimisation of the electrolyte parameters is outside the scope of this thesis, and the focus lies solely on the electrochemical stability and decomposition reactions of the electrolyte, and on what implications they have on LIBs.

An electrolyte consists at least of two parts, a solvent and a salt. A classic LIB electrolyte formulation is 1 M lithium hexafluorophosphate ($LiPF_6$) salt in a 1:1 volume mix of the organic solvents ethylene carbonate (EC) and diethyl carbonate (DEC). The salt, $LiPF_6$, is generally chosen for LIBs not because it excels at any particular property, but mainly because it can passivate the current collector of the positive electrode and performs relatively well across the board compared to other salts [10]. Still, drawbacks exist, and especially electrolyte acidification via HF formation is problematic as it accelerates cell degradation. Cyclic and linear carbonate esters, EC and DEC as respective examples, commonly serve as solvents in LIBs due to their high electrochemical stability and broad working potential range. Their polar nature also allows for the dissolution of substantial quantities of salt [10]. This thesis specifically investigates EC, the preferred cyclic carbonate solvent for LIBs due to its high compatibility with carbonaceous electrodes compared to EC analogues, *e.g.* propylene carbonate (PC) [11]. The addition of the linear carbonates extends the operating temperature range of the electrolyte as the melting point of the cyclic and linear carbonate solvent mix is lower than the high melting point of EC, resulting in an extended operating temperature range. Furthermore, linear carbonates mix homogeneously with EC and are stable to a similar extent as EC towards oxidation, which is not the case for many other possible co-solvents to EC [10]. The narrow selection of well-functioning salts and

solvents in commercial LIBs is primarily because of decomposition side reactions at the interface to the electrodes. Therefore, this area deserves our utmost attention.

1.2.2 Interphases and near-surface electrode regions

Electrochemistry occurs at the interface where the electrode meets the electrolyte. However, in the context of batteries, simply referring to a 2D interface does not adequately describe the electrochemistry situation at the electrode surfaces. Instead, the 3D terms "interphase" and "near-surface electrode region" are more apt. The interphase (Figure 1.2) describes a region that begins at the electrode surface and extends up to hundreds of nanometers towards the electrolyte solution. In this interphase region, the organic and inorganic products from decomposition reactions form a layer on the electrodes and can be seen as a separate phase in between the electrodes and electrolyte [12]. The near-surface electrode regions stretch from the electrode surfaces into the electrodes (Figure 1.2). The near-surface electrode regions are prone to initial structural changes when under enough stress, for example, exfoliation processes of a graphitic negative electrode [13] or when excessive quantities of Li^+ ions are removed from a transition metal oxide positive electrode, leading to structural collapse [14].

Figure 1.2 shows typical processes that can occur in the interphases and the near-surface electrode regions for the negative and positive electrodes. In a perfect situation, none of these processes would take place. However, in practice, they cannot all be avoided, but many can be mitigated, *e.g.* by choosing a suitable electrolyte solution, including beneficial electrolyte additives or us-
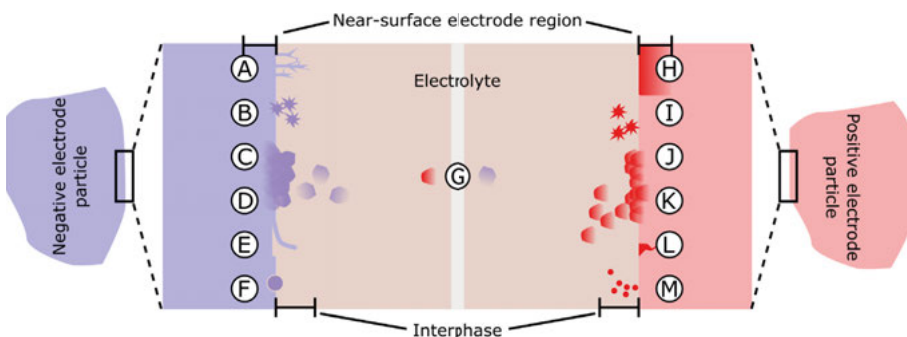
Figure 1.2. Schematic of select processes occurring at the electrode/electrolyte interphases and near-surface electrode regions of LIB cells. A. Dendrite formation, B. Electrolyte reduction, C. Solid electrolyte interphase (SEI) formation, D. SEI dissolution, E. Exfoliation, F. Junk formation, G. Cross-talk, H. Structure changes, I. Electrolyte oxidation, J. Cathode electrolyte interphase (CEI) formation, K. CEI dissolution, L. Cracking, M. Transition metal dissolution.

16

ing careful cycling protocols. A LIB can achieve high coulombic efficiency[ii] (>99.9%), but the final percentile is lost due to detrimental side reactions accumulating over time and putting a best-before date on LIBs [15].

1.2.3 Solid Electrolyte Interphase

A focus point in this thesis is to understand detrimental side reactions, and subsequently how they can be mitigated at the negative electrode. The interphase at the negative electrode in LIBs is comprised of the 'necessary evil' solid electrolyte interphase, SEI (Figure 1.2, process C), which suppresses other detrimental interphase processes [16, 17], but also increases the electric resistance of the cell.

The SEI typically derives from electrolyte reduction at the negative electrode whereby some of the decomposition products precipitate on the electrode surface to form a protective layer separating the electrode and the electrolyte. Without an SEI the LIB cell's lifespan is significantly reduced due to continuous electrolyte decomposition, which quickly results in cell failure [9, 18, 19].

The SEI should fulfil three base functions for a battery cell to remain functional if it operates at potentials where the electrolyte is reduced. First, an electronically insulating layer covering the whole negative electrode is needed to separate the electrolyte solution from the highly reductive negative electrode surface, which mitigates further electrolyte decomposition after the initial SEI formation. Second, Li^+ ion conductivity must be retained for reversible Li^+ ion transfer between the negative electrode and the electrolyte. Third, the SEI must not dissolve into the electrolyte. Other desirable properties of the SEI may vary, depending on the specific application of the LIB. However, an effective SEI should generally exhibit flexibility, thinness, homogeneity, minimal contribution to cell resistance, thermal stability, and prolonged lifetime [9].

Despite playing an important role in LIB performance, the SEI has some drawbacks that need to be controlled and minimised. First, some Li^+ ions from the positive electrode are irreversibly lost during the SEI formation process, lowering the total cell capacity, as the formed SEI products consume Li^+ ions. Second, higher cell resistance is introduced to the system when the SEI forms [20, 21]. Third, the SEI continuously grows during usage, further lowering the total cell capacity [22]. Consequently, the understanding and engineering of the SEI is crucial to enable optimal performance conditions in LIBs.

The SEI was first described by E. Peled in 1979: " ...in practical nonaqueous battery systems the alkali and alkaline earth metals are always covered by a surface layer... This layer is formed instantly by the contact of the metal with the solution... This layer consists of some insoluble products of the reaction of the metal with the solution. It acts as an interphase between the metal and the

---

[ii]The ratio between total charge put into and extracted from a battery during a full charge-discharge cycle.

solution and has the properties of solid electrolyte, through which electrons are not allowed to pass. Therefore, it is called Solid Electrolyte Interphase (SEI)." [23]. The SEI concept was later applied to Li-ion batteries, beginning with studies by Fong et al. [24].

Since Peled's initial description, various models have been proposed to understand the SEI structure and working mechanism, with three early models laying the foundation. In 1982, Geronov et al. introduced a bi-layer SEI model consisting of an inner protective layer and an outer porous layer [25]. Following this, in 1996, Zaban et al. presented a multilayer SEI model, characterised by distinct SEI layers [26]. In 1997 Peled et al. proposed a mosaic SEI model, suggesting the coexistence of multiple phases in the interphase region [27]. With the rapid advancement of analytical instruments since these initial models, numerous updates have been proposed to enhance our understanding of the SEI [19, 28]. However, many of these newer models still bear resemblance to the original concepts, and depending on the specific battery system studied, the original models continue to hold relevance.

The SEI is well-acknowledged to be typically comprised of a mix of inorganic and organic species. In state-of-the-art LIBs, the most agreed-upon composition model of the SEI is that inorganic SEI components are more concentrated near the negative electrode surface, while SEI farther from the surface are richer in organic species [27, 29, 30].

Although the SEI plays a critical role in the performance and longevity of LIBs, several challenges persist to fully understand and characterise it. One key issue is that the SEI is dynamic, undergoing changes not only during the battery's operation but also potentially during the battery cell disassembly process and subsequent *ex situ*[iii] analyses [31]. Furthermore, the SEI is a nanometer-thin film [32–35], challenging even the most advanced analytical techniques to achieve the necessary sensitivity and accuracy in their results. Additionally, the formation and characteristics of the SEI are influenced by handling conditions and cycling protocols, complicating the comparison of research findings across different studies [31, 36]. In light of these challenging conditions, it is no wonder that the SEI remains elusive to us.

1.2.4 Electrolyte additives

The development of LIB electrolyte solutions has increasingly focused on the advancement of additives in recent years as they can fulfil requirements that the base electrolyte cannot achieve. Electrolyte additives are functional molecules dissolved in the electrolyte and enhance the performance of the LIB. Typically, additives chosen for LIB are more selective in their reactivity than the base electrolyte components and are largely consumed in sacrificial processes [9, 37].

[iii]Sample to be analysed is extracted from the system it was operating in.

Additives can be categorised into different types based on their functions. Layer-formers improve the SEI [38] and cathode electrolyte interphase (CEI) [39], by decomposing and forming a layer on the electrodes, directly influencing the interphase by affecting one of the properties stipulated in Chapter 1.2.3. Examples of layer-forming additives explored in this thesis and improving LIB performance are vinylene carbonate (VC) and lithium bis(oxalato)borate (Li-BOB).

Scavenging additives, on the other hand, have a more indirect effect as they target and neutralise impurities that negatively affect the interphase, such as HF and H_2O [40]. This type of additive is beneficial as a more controlled SEI formation is possible due to the reduced amount of residual contaminant reactants in the system. Two example additives with this property are VC and tris-(trimethylsilyl)phosphate (TMSPa) [41].

Beyond the layer-former and scavenger additive categories are for example stabilisers and flame-retardants [37]. However, these are outside the scope of this thesis and are not discussed further.

Monitoring additive reactions can pose challenges when solely relying on electrochemistry due to their tendency to follow chemical rather than electrochemical reaction pathways. Therefore, complementary techniques to electrochemistry are needed for a better understanding of additives. Fortunately, many additives produce gas as a reaction byproduct, and monitoring the gas can provide valuable insights into the reaction pathways of the additives.
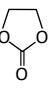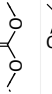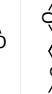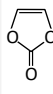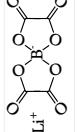
1.2.5 Gas evolution in LIBs

The gas-evolving reactions in LIBs are important to monitor and understand as they affect the LIB performance and tell much about processes taking place in LIBs that are hardly distinguishable in the electrochemical data. All LIBs experience gas evolution, mainly during the formation cycles[iv], where the electrode/electrolyte interface is conditioned (*e.g.* SEI formation) before normal charge and discharge usage.

The working voltage window of state-of-the-art LIBs is wide enough that electrolyte decomposition is inevitable. As a result, decomposition products will form, and some are gases. Processes generating gas in LIBs are to a large extent interphasial reactions described in Figure 1.2, either as a direct result or due to subsequent reactions. What gases evolve from a battery cell and how much depends on the choice of electrodes, electrolyte solutions (solvent, salt and additives), and cycling protocol. Table 1.1 is a collection of herein-studied LIB solvents, salts, additives, and residual contaminants and the various gases they can produce under different conditions during formation cycles. The possible reactions contributing to gas evolution in LIBs are further discussed in Chapters 3-5.

[iv]First few cycles after cell assembly.

Table 1.1. *Common LIB compounds (solvents, salts, additives and residual contaminants) and their respective evolving gases reported during decomposition processes that are achievable within an operating battery cell. Each column header represents what is needed to produce gas from each compound. A dash (-) corresponds to no gases evolving at that specific combination or that they have not been studied/published concerning batteries. Reduction is $+e^-$, oxidation is $-e^-$, $+NU^-$ is a nucleophile, and $+\Delta T$ is elevated temperature, and $+H_2O$ is residual water. Gas evolution marked with a star (*) indicates that favourable conditions are needed, such as specific electrode materials or a combination of this table's columns. References marked with a double star (**) indicate that the results are in contradiction with the reference following the double star, and the source of the gas may originate from a different process.*

Compound	Structure/ formula	$+e^-$	$-e^-$	$+NU^-$	$+\Delta T$	$+H_2O$
Ethylene carbonate (EC)		C_2H_4, CO [42–45]	CO_2, CO [46–49]	CO_2 [36, 43, 50]	CO_2, CO [45]	CO_2* [50]
Linear carbonates (DMC, DEC, EMC)		CH_4, C_2H_6, C_2H_8, CO, CO_2 [45, 49, 51–54]	CO_2, CO [46]** [55]	-	CO_2 [45]	-
Propylene carbonate (PC)		C_3H_6 [11, 53, 56]	CO_2* [57]	H_2* [56]	-	-
1,2-dimethoxyethane (DME)		-	-	-	-	-
Vinylene carbonate (VC)		CO_2 [58]	CO_2 [47, 59]	CO_2 [58]	-	-
Lithium hexafluorophosphate	$LiPF_6$	-	PF_5/POF_3 [60]	PF_5/POF_3 [46, 61]	PF_5/POF_3 [62, 63]	PF_5/POF_3 [64]
Lithium perchlorate	$LiClO_4$	-	CO_2*,CO* [60]	-	-	-
Lithium bis(oxalato)borate (LiBOB)		CO_2 [65]	CO_2 [39]	-	-	-
Water	H_2O	H_2 [43, 44]	CO_2*, CO* [66]	-	-	-
Hydrofluoric acid	HF	H_2 [36, 67]	-	-	-	-

1.3 Residual gas electron ionisation quadrupole mass spectrometry

A mass spectrometer (MS) is a very precise balance, where ions can be separated and detected based on their mass-to-charge ratio (m/z), or m/z channel, by manipulating the ions' trajectory in an electromagnetic field. Numerous MS variations have been developed since its invention at the turn of the 20th century [68]. Still, mass spectrometry (MS) at its core consists of an ionisation source, a mass filter and a detector under vacuum. An overview of a quadrupole MS that is based on electron ionisation is shown in Figure 1.3.

First, the sample of interest needs to be extracted and transported to the inlet of the MS (Figure 1.3 – process A). This process can be achieved, *e.g.* via headspace extraction, where one end of a capillary is connected to a closed volume with sample gas and the other end of the capillary to the inlet of the MS. The capillary works as a pressure reducer between the volume of sample gas and MS, ensuring a low operating pressure inside the MS.

The second step of the MS analysis is to ionise the introduced sample of interest (Figure 1.3 – process B). Ionisation techniques vary, ranging from hard to soft ionisation. Hard ionisation is generally non-selective and typically causes extensive fragmentation of the introduced sample gas. Samples with limited possible fragmentation are ideally ionised by hard ionisation, such as electron ionisation (EI). The gases analysed in this thesis (see Table 1.1) are all in general favourably ionised with EI. The process of EI involves heating a filament, which then emits electrons. When sample gases, introduced into the chamber (*e.g.* through a capillary), come into contact with these electrons, they become ionised and, to a certain extent, fragmented. This ionisation allows for electromagnetic extraction of the sample. Subsequently, the ions are
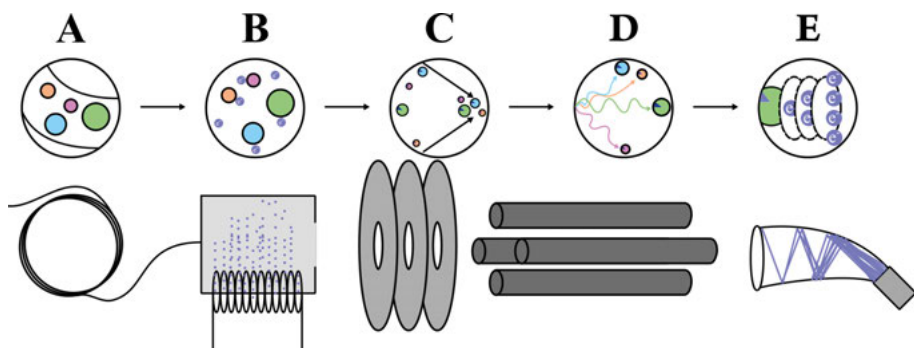
Figure 1.3. A schematic working principle of an MS, where each bubble is a magnification of the processes A-E. A. Gas is introduced via a capillary. B. Gas is ionised by the ionisation source. C. Ionised gas is extracted and focused. D. (Quadrupole) mass filter confines only ionised gas species with specific m/z to a stable travel path. E. Species with stable travel path hit (electron multiplier) detector, generating an output current, so-called ion current.
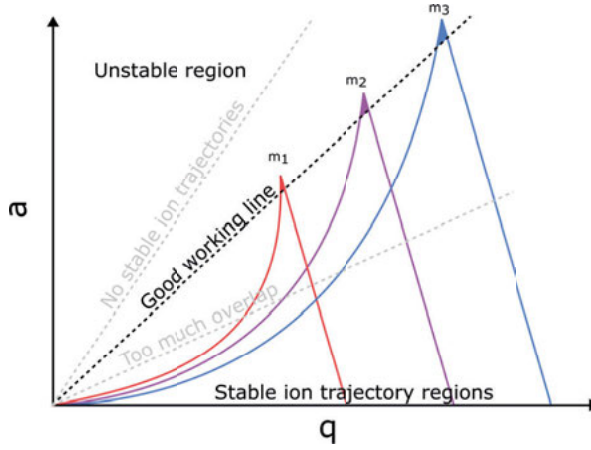
Figure 1.4. Stability diagram of the quadrupole working line with stability parameters a and q. The coloured areas of each mass ($m_1 - m_3$) represent how each mass is allowed through the quadrupole one at a time.

focused and accelerated towards the mass filter (Figure 1.3 – processes C), the next step of MS analysis.

A common mass filter used in MS is the quadrupole consisting of four metal rods subjected to an oscillating voltage (Figure 1.3 – process D) [69]. Two opposite rods have a positive voltage (U) applied, and an alternating voltage (V) on top of U. The other two opposite rods have a negative U applied, and similarly V added on top. The varying electromagnetic field acts as a filter and discriminates "too light" and "too heavy" ions, resulting in unstable ion trajectories except for the ions with a specific m/z value. A stability diagram (Figure 1.4) visualises how different ion masses can be separated by changing the slope of the MS "working line". The stable ion trajectory regions show the needed conditions for each ion mass to achieve a stable oscillation. However, for the ions to pass through the quadrupole, they need to be above the working line of the MS. The stability parameters "a" and "q" are dimensionless variables, which are tuned to change the m/z value with a stable trajectory. The stability parameters are determined by Mathieu's differential equations.

$$a = \frac{8eU}{mr_0^2\omega^2} \tag{1.2}$$

$$q = \frac{4eV}{mr_0^2\omega^2} \tag{1.3}$$

Only U and V are normally changed during a measurement. The remaining parameters, e (ion charge), m (ion mass), r_o (distance from the quadrupole centre to the surface of any rod), and ω (angular frequency of the applied ac waveform) are constant.

Finally, after the mass filter, the sample ions reach the detector (Figure 1.3 – process E), a Faraday cup or a continuous secondary electron multiplier (C-SEM). A C-SEM detector is used when small ion currents are measured and a high signal-to-noise (S/N) ratio is needed. The sample ions hit the detector, and the resulting detector current is multiplied through a cascading process. Calibration is needed regularly as the C-SEM ages with use, and because the conversion factor differs depending on the sample ions' mass, which introduces an error in quantification studies if the detector is left uncalibrated.

1.4 *Operando* gas analysis of batteries

Analysing the evolving gases in an electrochemical system is beneficial as both qualitative and quantitative data can be gathered regarding reaction pathways and their kinetics [70, 71]. While extracting gas after an experiment (*ex-situ*) can tell much about a system, pinpointing onsets, separating different processes, and identifying possible intermediary steps in real-time gives a better holistic understanding of the studied system [70]. Processes like SEI formation are especially well suited for *operando* studies as the SEI forms and changes during the operation of a battery [72, 73].

1.4.1 OEMS and DEMS

Online Electrochemical Mass Spectrometry (OEMS) and Differential Electrochemical Mass Spectrometry (DEMS) are conventional terms for instruments studying the gas phase of electrochemical systems *operando* with MS. Commercial *operando* gas instruments are limited, but the LIB research field features a variety of custom-made solutions [43, 74–79]. This diversity has led to a complex naming convention, and OEMS and DEMS are often used interchangeably despite the custom-made solutions having different working principles, requirements and limitations.

OEMS serves as an umbrella term for *operando* gas analysis in electrochemical devices, with DEMS being a specific category within it. DEMS originally used a membrane in contact with the electrode and electrolyte, extracting gases through it, and the extracted gas had to go through differential pressure reduction before being introduced to the MS. Nowadays, differential pumping is not a criterion for DEMS, but all gases are extracted as soon as they evolve. In contrast, other OEMS systems, like Purging Online Electrochemical Mass Spectrometry (POEMS) and Intermittently Closed Electrochemical Mass Spectrometry (ICEMS), rely on headspace analysis using a capillary for pressure reduction [80], allowing most of the evolved gases to remain inside the cell but extending retention times from milliseconds to tens of seconds or more. This type of headspace analysis is generally named OEMS in published literature [76–79, 81].

Headspace OEMS and DEMS have advantages and disadvantages compared to each other, and the best-suited technique is determined by what system the user is about to study. However, headspace OEMS is generally better suited for batteries compared to DEMS, since gas analysis experiments of batteries can stretch up to several days. Therefore, the retention time is less important to consider, but the gas composition of the battery cell is less tampered with, resulting in a system more similar to a commercial cell.

2. Methodology

2.1 Online Electrochemical Mass Spectrometry

Figure 2.1 shows a schematic of the OEMS instrument developed and applied throughout this thesis work. In principle, the instrument consists of three sections with their respective gas volumes:

1. Electrochemical gas cell and pressure sensor: Cell volume (V_c)
2. MS: Analysis volume (V_a)
3. Carrier and calibration gas: Manifold volume (V_m)

The volumes are divided into sections (green, blue and purple) by solenoid valves, which open and close depending on where the gas should flow or what volume needs to be pumped to vacuum. The three sections are described in further detail in Chapters 2.1.1-2.1.3.

2.1.1 Electrochemical gas cell and pressure sensor: V_c

Efficient gas analysis requires a dedicated electrochemical cell including a gas headspace, which can be purged via a gas inlet and outlet. Figure 2.2 shows a schematic and a picture of the custom-made cell. The electrochemical gas cell is composed of a stainless steel bottom and top lid. To ensure a gas-tight
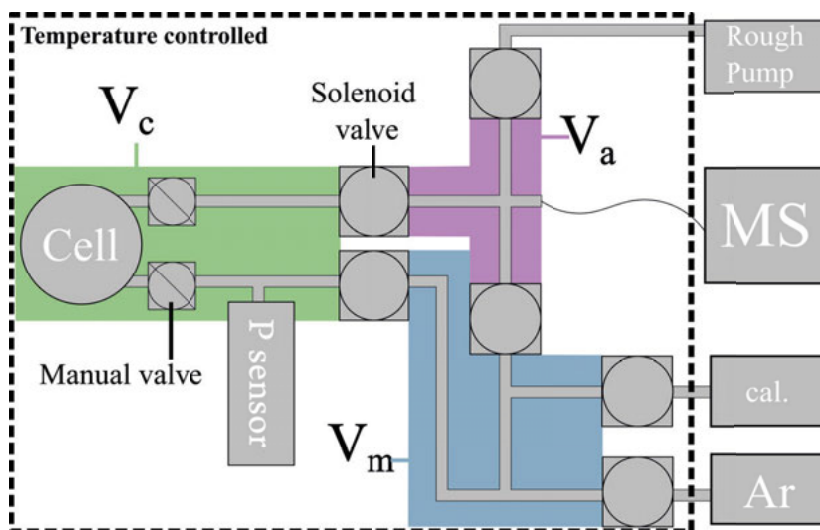

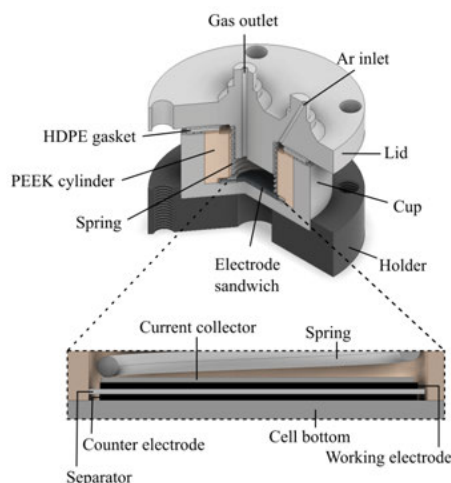*Figure 2.1.* Schematic of the custom-made OEMS instrument.

Figure 2.2. Schematic (left) and picture (right) of the electrochemical gas cell.

and electrically insulating seal, a high-density polyethylene (HDPE) gasket is placed between the lid and bottom, which are then fastened together using screws that insert into a polyoxymethylene holder. Located on the lid are the gas inlet and outlet. Manual valves are welded to the inlet and outlet connections on the exterior of the lid to maintain an inert atmosphere within the cell during transport from an Ar-filled glovebox to the OEMS instrument. These valves are fitted with metal gasket connections, facilitating the cell's integration with the OEMS instrument. Inside the lid, the gas inlet and outlet are positioned as far apart as possible, with the outlet near the working electrode. This design ensures that gases evolving from the electrode are sampled rather than the fresh Ar entering through the inlet.

A polyether ether ketone (PEEK) inner lining encircles the electrode sandwich inside the cell bottom. The PEEK inner lining is either an open cylinder or a cup, where a stainless steel puck is force-fitted to the bottom of the PEEK inner lining to prevent the electrolyte from flowing away from the electrodes. The electrode sandwich is centred inside the PEEK lining, and the working electrode is always on top to ensure a direct route for evolved gas to the cell headspace. A stainless steel spring connects the working electrode with the lid, and the counter electrode is in contact with the cell bottom to complete the circuit.

A temperature and total pressure sensor is also included in V_c. The temperature is continuously monitored to ensure stable experiment conditions are maintained inside V_c. The pressure in V_c is monitored continuously in the absolute range of 0.8-1.2 bar with an encapsulated piezoresistive sensor. The achieved accuracy is $\pm 0.05\%$ (0.6 mbar) of full scale between +10 °C and

+40 °C and ±0.1% (1.2 mbar) of full scale between -10 °C and +80 °C. The operating pressure in V_c is kept between 1.10-1.15 bar absolute pressure but varies within the range depending on experiment parameters such as the climate chamber temperature, the volume evolved gas from the OEMS experiment, and the ambient temperature.

2.1.2 Mass spectrometer: V_a

The MS used in the OEMS instrument is equipped with a closed EI source, quadrupole analyser, and C-SEM detector, which are described in Chapter 1.3. The MS is connected to a turbo-pumping unit to achieve the required vacuum levels ($<10^{-5}$ mbar). V_a is the MS antechamber volume where extracted gas from V_c is temporarily stored at ca. 1.1 bar during MS measurement points. Fractions of the V_a gas mixture are introduced to the MS via a heated (60 °C) fused silica capillary. The low flow rate of the capillary ($\sim 12\,\mu$L/min) results in a pressure reduction between V_a and the MS chamber to achieve a good working pressure for the MS in the upper 10^{-6} mbar range. V_a is pumped to vacuum using a rotary vane pump in between every measurement point, resulting in an idle pressure $<10^{-8}$ mbar in the MS chamber. Pumping to idle pressure between measurement points prolongs the lifetime of the filament and detector. Additionally, the pumping and flushing of V_a before measurement points ensure minimal influence on the subsequent measurement point.

2.1.3 Carrier and calibration gas: V_m

All gases needed during OEMS measurements and C-SEM calibration are accessed via V_m. During a measurement – V_c is refilled with an inert carrier gas (Ar, purity 99.9999%) via V_m every time gas is extracted for an MS measurement point. V_m is kept in an over-pressured Ar atmosphere (1.1 bar absolute pressure) during idle conditions and flushed with carrier gas before a measurement point to ensure as high purity Ar as possible is refilled into the electrochemical cell.

   The calibration gases used for the OEMS instrument are 2000 ppm O_2 in Ar, a mix of 2000 ppm CH_4 and C_2H_4 in Ar, and a mix of 2000 ppm H_2 and 4000 ppm CO_2 in Ar. The calibration gases are stored separately from each other to avoid overlapping MS signals during calibration. V_m is flushed with each calibration gas until a stable signal is reached to ensure proper C-SEM calibration. The calibration procedure is described in Chapter 2.1.5.

2.1.4 Softwares

Three different software are needed to run an OEMS experiment. First, a Labview-compatible MS Application Programming Interface (API, from Pfeif-

fer Vacuum Technology AG). The API is used for MS setup and internal MS calibration (*e.g.* filament potential and detector gain), as well as real-time extraction of data. Second, any cycling equipment, and its dedicated software can be used to control the desired cycling protocols. Finally, the OEMS instrument is controlled by a custom-made Labview software, that enables automatic gas sampling of the electrochemical gas cell. The program handles any solenoid valve operation and synchronises data collection from MS, pressure sensors, and cycling equipment. The pressure sensor has compatible Labview functions available, meaning no dedicated software is needed for the sensor to function.

2.1.5 MS calibration

The output from the MS is generated ion currents for each m/z channel monitored. Each sample molecule generates its unique mass spectrum and can be identified from the ion currents. However, the sensitivity for each gas species will vary between MS instruments. Therefore, calibration is needed for quantitative analysis. Also, species are regularly introduced at the same time, resulting in overlapping mass spectra, which can only be reliably deconvoluted with proper calibration.

Two calibration processes are used to calibrate the MS. The first process is the baseline calibration of the C-SEM detector where calibration gases (listed in Chapter 2.1.3) are used to link the concentration of the individual calibration gases to certain ion current signal magnitudes. The working principle of the baseline calibration protocol follows. First, V_m and V_a are flushed with pure Ar carrier gas. Then, V_a is filled with Ar gas and the ion currents for the m/z channels of interest are recorded to determine the individual m/z channel background signals. Next, V_a is flushed with a calibration gas at a time and the m/z channels of interest are recorded. Now, the background signal (b) and calibration gas concentration (x) are linked to a certain ion current magnitude (I). This procedure is repeated for all calibration gases to calculate calibration values (S) for each calibration gas contributing to m/z channels of interest. The full calibration is described by the matrix equation:

$$\hat{I} = \bar{S}\hat{x} + \hat{b} \tag{2.1}$$

Which expanded looks like:

$$\begin{bmatrix} I_1 \\ I_2 \\ \vdots \\ I_n \end{bmatrix} = \begin{bmatrix} S_{1,1} & S_{1,2} & \cdots & S_{1,n} \\ S_{2,1} & S_{2,2} & \cdots & S_{2,n} \\ \vdots & \vdots & \ddots & \vdots \\ S_{n,1} & S_{n,2} & \cdots & S_{n,n} \end{bmatrix} \begin{bmatrix} x_1 \\ x_2 \\ \vdots \\ x_n \end{bmatrix} + \begin{bmatrix} b_1 \\ b_2 \\ \vdots \\ b_n \end{bmatrix} \tag{2.2}$$

Where $\hat{I}$ is the generated ion currents for all monitored m/z channels, $\bar{S}$ is the calibration matrix, $\hat{x}$ is the concentration of the different calibration gases, and $\hat{b}$ is the background vector for the monitored m/z channels.

During baseline calibration, $\bar{S}$ is updated so $\hat{I}$ reflects the correct calibration gas concentrations ($\hat{x}$). $\bar{S}$ considers all fragments showing up on the different monitored m/z channels from each gas species and enables the separation of every individual gas contribution to an overlapping m/z channel. An example of $\bar{S}$ is seen in Table 2.1. The sensitivity matrix and background vector need to be updated regularly as the MS ages. The baseline calibration is done without any solvents present. This way only the pure calibration gas is accounted for in a 'blank' sampling system. However, the volatile components of the electrolyte solution need to be considered during an OEMS experiment, as it will affect the magnitude of the generated ion currents for each gas of interest to different degrees. Therefore, a second calibration process is needed to achieve a solvent-specific calibration.

The second calibration process is done post-experiment. Both ion currents and total cell pressure ($\Delta P V_c / RT$) are converted into gas evolution rates (described in Chapter 2.1.7) to compare them to each other. The sum of all MS monitored gases ($\Sigma \Delta n$) should correspond to the total pressure change. The electrolyte solvents used in the OEMS experiment are monitored on separate m/z channels, which are used to update $\hat{b}$ and $\bar{S}$ to be solvent-specific. During the $\bar{S}$ fitting process, partial pressure magnitudes are fitted to the total pressure by changing the electrolyte solvent calibration. The result is a better overlap of the sum of all partial pressures and the total pressure, as exemplified in Figure 2.3.

A series of experiments with similar parameters (*e.g.* temperature, electrodes and solvents) should rely on the same $\bar{S}$ and fitting protocol for the second calibration to be comparable. Additionally, a qualitative understanding of the studied system is a prerequisite, as most of the evolving gases need to be known. In case there is a peak in the total pressure that cannot be fitted with the monitored partial pressures, then there is an unknown gas that needs to be identified and monitored.

Table 2.1. *Example S matrix with each gas species' relevant fragments marked.*

m/z	H_2	CH_4	C_2H_4	CO	O_2	Ar	CO_2	$\cdots$
2	$S_{1,1}$	0	0	0	0	0	0	$\cdots$
15	0	$S_{2,2}$	0	0	0	0	0	$\cdots$
26	0	0	$S_{3,3}$	0	0	0	0	$\cdots$
28	0	0	$S_{4,3}$	$S_{4,4}$	0	0	$S_{4,7}$	$\cdots$
32	0	0	0	0	$S_{5,5}$	0	0	$\cdots$
36	0	0	0	0	0	$S_{6,6}$	0	$\cdots$
44	0	0	0	0	0	0	$S_{7,7}$	$\cdots$
$\vdots$	$\vdots$	$\vdots$	$\vdots$	$\vdots$	$\vdots$	$\vdots$	$\vdots$	$\ddots$

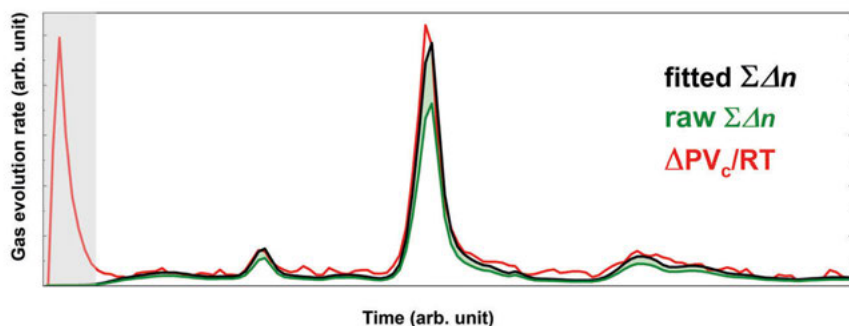*Figure 2.3.* Second calibration after an OEMS experiment. The raw sum of MS-determined partial pressures converted to gas evolution rate (ΣΔn) is fitted to the total pressure profile ($\Delta PV_c/RT$) determined by the integrated pressure sensor in V_c. The area shaded in green is the difference between raw and fitted ΣΔn after the second calibration. No current flows through the cell in the area shaded in grey and the cell temperature is stabilising.

2.1.6 Data collection

OEMS data is collected from three sources – pressure (and temperature) sensor, potentiostat(/galvanostat), and MS. The pressure sensor and potentiostat collect data continuously. However, the pressure profile is disrupted every time gas is extracted from V_c to V_a, and when V_c is subsequently filled with fresh Ar gas. The result is a periodic pressure behaviour, shown in Figure 2.4, and the pressure shifts several mbars for every MS measurement point. Tens of seconds are needed for the pressure to stabilise after a measurement point, which is labelled as P' and used as the starting pressure of a measurement cycle. The difference between P' and the pressure moments before the next measurement point (P) translates to the total gas evolution during a measurement cycle (the mathematical expression is described in Chapter 2.1.7). In other words, even though the pressure data is collected continuously – discrete pressure values are used to calculate the total pressure.

The experiment-specific MS data is collected discretely. The gas mixture in the electrochemical gas cell headspace is probed at user-set intervals for a measurement point according to the following procedure. First, V_m and V_a are flushed with Ar before any measurement point, and V_a is left under vacuum. Then, the extracted gas mixture from V_c enters V_a, where gases are monitored by the MS for a user-set number of multiple ion detection (MID[i]) cycles. The recorded data point is an arithmetic average of each m/z channel over the last ten MID cycles. The total number of MID cycles exceeds the number needed

---

[i]MID is a common MS sampling method. Specific m/z channels are monitored in the MID method, resulting in higher achieved sensitivity compared to the scan method. All m/z channels in a certain range are monitored but with lower sensitivity in the scan method.
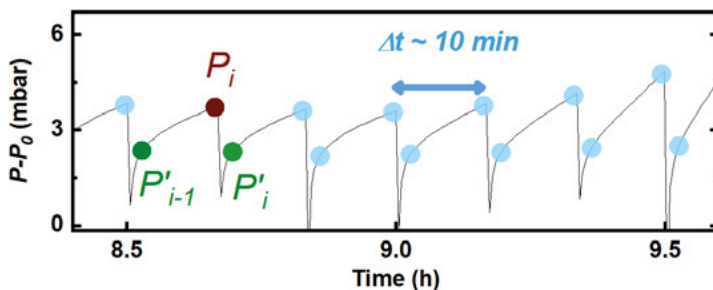
Figure 2.4. Pressure profile during periodic gas sampling from the electrochemical cell every 10 minutes. Every dot (blue, green and brown) is a pressure value used to calculate the total pressure in the cell.

for the recorded data point because the ion currents need to stabilise and the gas in V_a need to be given time to homogeneously mix. An example of the ion current signals during a measurement point is shown in Figure 2.5. Finally, when the ion currents are recorded, V_a is flushed with Ar and pumped to a rough vacuum level.

2.1.7 Data analysis

The output, ion currents (in ampere) from the MS, need to be treated for easier comparison with each other, and the total pressure from the pressure sensor. The generated MS ion currents and the total pressure changes are normally converted to gas evolution rates for comparison throughout this thesis work. The ion currents are first converted to partial pressures (gas concentrations) by solving equation 2.1 with regards to $\hat{x}$. Then, the partial pressures are converted into gas amounts by solving the Ideal Gas Law with regards to the number of mols (n):

$$n = \frac{xPV}{RT} \tag{2.3}$$

Where x is the gas concentration, P is the cell pressure, V is the cell volume, R is the gas constant and T is the temperature. However, additional considerations are needed to describe the gas evolution reliably. The volume of extracted gas at every measurement point must be considered to achieve a proper description of the V_c headspace gas composition. Then, the sampling time is used to convert the mols into a rate of mol/[time unit]. The full equation converting partial pressures (calculated from Equation 2.1) into gas evolution
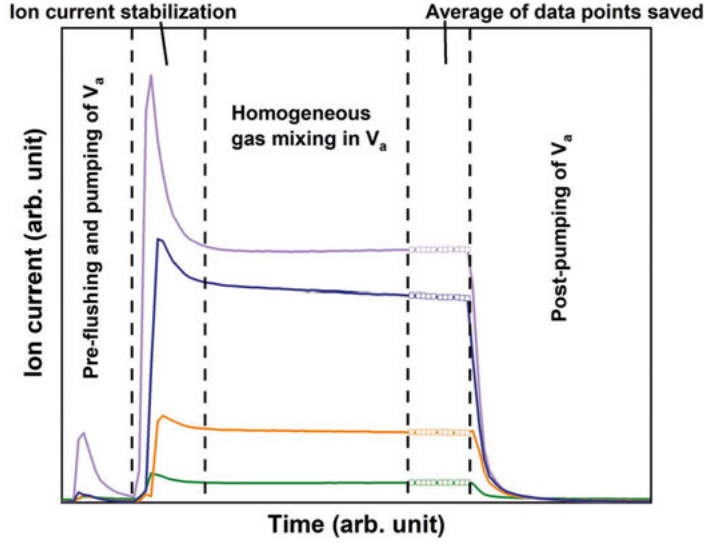
31

Figure 2.5. Example of ion current profiles during an OEMS measurement point. Each coloured line represents a different monitored m/z channel. The working principle is as follows (from left to right in the figure). First, V_a is flushed and pumped before any gas is extracted from the electrochemical gas cell. Then, the extracted gas mixture is analysed long enough for all ion currents to stabilise and ensure a homogeneous gas mix in V_a. The average of the final ten data points for each m/z channel are saved. Finally, V_a is pumped to vacuum by the rough pump.

rates and considering extracted gas is described by:

$$
\begin{aligned}
\hat{k}_i^{MS} &= \frac{\Delta \hat{n}_{i,i-1}^{MS}}{\Delta t_{i,i-1}} \\
&= \frac{\hat{n}_i - (\hat{n}_{i-1} - \hat{n}_{i-1,a})}{t_i - t_{i-1}} \\
&= \frac{\frac{\hat{x}_i P_i V_c}{RT} - \hat{x}_{i-1}\left(\frac{P_{i-1}V_c}{RT} - \frac{P'_{i-1}V_a}{RT}\right)}{t_i - t_{i-1}} \\
&= \frac{1}{RT} \frac{\hat{x}_i P_i V_c - \hat{x}_{i-1}(P_{i-1}V_c - P'_{i-1}V_a)}{t_i - t_{i-1}}
\end{aligned}
\tag{2.4}
$$

$\hat{k}_i^{MS}$ is the average gas evolution rate for the monitored gases between measurement points i and i-1. $\Delta \hat{n}_{i,i-1}^{MS}$ is the difference in the number of mols between two measurement points, and $\hat{n}_{i-1,a}$ accounts for the extracted number of mols gas from the previous measurement point. P is the pressure before a measure-

32

ment point, and P' is the pressure after a measurement point (see Figure 2.4). $\hat{x}$ is the gas concentration for the individual gases.

The total pressure conversion into gas evolution rate also utilises the Ideal Gas Law, and expanded looks similar to equation 2.4:

$$
\begin{aligned}
\hat{k}_i^{PT} &= \frac{\Delta n_{i,i-1}^{PT}}{\Delta t_{i,i-1}} \\
&= \frac{\Delta P V_c}{RT} \frac{1}{\Delta t_{i,i-1}} \\
&= \frac{V_c}{RT} \frac{P_i - P_{i-1}'}{t_i - t_{i-1}}
\end{aligned}
\tag{2.5}
$$

However, $\hat{k}_i^{PT}$ does not have to consider the extracted gas. Instead, the calculation is based on the first and last pressure values from the pressure sensor data in a measurement cycle (see the difference between P_{i-1}' and P_i in Figure 2.4).

2.1.8 Single vs. multi-cell instrument

Many advanced analytical instruments, including OEMS, face the challenge of being time-consuming, making it difficult to run extensive experiment matrices with adequate replicates for robust conclusions. However, since the OEMS instrument developed and used herein relies on periodic sampling, three cells can effectively run concurrently with staggered MS measurements, significantly increasing experimental throughput. As a result, a larger experimental matrix can be completed in a shorter timeframe.

Running a multi-cell OEMS instrument, however, requires some considerations to ensure high-quality data is produced. First, cross-contamination between cells must be prevented. Additional flushing of the volumes V_a and V_m is necessary to ensure that residual gases from other cells are thoroughly removed. Still, volatile components, such as electrolyte solvents, are difficult to pump out completely as they tend to stick to the surfaces of the OEMS. Any residual solvent in V_a or the capillary will affect the solvent background and $\bar{S}$ in the calibration matrix. Therefore, any cells running concurrently should use the same electrolyte composition to ensure a stable background is achieved. Second, as the instrument's complexity and the number of components increase, so does the need for maintenance.

2.2 Considerations for *operando* gas analysis of batteries

Instrument-specific considerations are always needed to operate an analytical instrument. However, for *operando* techniques, and especially for custom-

made instruments, the methodology and experiment parameters need to be validated carefully before relying on any results. Here are the preparatory steps, sensitivity limit, sources of noise, and needed result considerations for *operando* gas analysis discussed.

In any OEMS experiment, several preparatory steps are required. First, the working electrode needs to be accessed unobstructed by both the electrolyte solution and cell headspace to ensure a direct route for both ions in the electrolyte to the electrode surface, and evolving gases from the electrode surface to the headspace. Otherwise, delays in the instrument are to be expected, either by sluggish Li$^+$ ion transport or by gases needing to diffuse longer distances to reach the headspace. Therefore, mesh current collectors or free-standing composite electrodes are suitable because they allow gases and ions to permeate freely through the porous electrode. Foil current collectors should generally be avoided, unless modified, *e.g.* by laser cutting holes in the foil to facilitate free movement of ions and gas through the electrode and current collector. The standard sampling time for OEMS measurements in this thesis is set to 10 minutes. A diffusion time for gases to reach the headspace can be estimated by:

$$ t \approx \frac{x^2}{2D} \tag{2.6} $$

Where t is the time, x is the distance evolved gas has to travel to reach the headspace and D is the diffusion constant. The calculated time for gas to reach the headspace in a $\sim$100 μm thick electrode, with 300 μm estimated distance for gas to travel to the headspace and a diffusion constant on the scale of 10^{-10}m^{2}s^{-1} is 7.5 minutes, which is lower than the 10 minutes sampling time. In the case a shorter sampling time is needed, it should be changed only after confirming that the gas diffusion is fast enough for the intended study. As a result, slow cycling (*e.g.* C-rate of C/10[ii] or scan rate of 0.1 mV/s) during OEMS is a soft requirement to ensure enough data points are gathered in a cycle to properly deconvolute gas evolution reactions.

Another preparatory step is that the volume of V_c must be known to convert the MS and pressure sensor output signals into comparable gas evolution rates, *e.g.* mol/min (as described in Chapter 2.1.7). Boyle's law says that the volume (V) and pressure (P) are inversely proportional for a gas with unchanged mass in a system at constant temperature.

$$ PV = \text{constant} \tag{2.7} $$

This can be used to calculate a volume when a fixed amount of gas expands into a new volume where the initial and final pressure is known as well as one of the volumes:

[ii]C-rate is a measure of how fast a battery is fully discharged relative to its maximum capacity. C/10 translates to the current needed to fully discharge a battery cell in 10 hours.

$$V_1 P_1 = V_2 P_2 \tag{2.8}$$

Where V_1 and P_1 are the initial volume and pressure, respectively. V_2 and P_2 are the final volume and pressure, respectively. The same equation is used to calculate V_c before an OEMS experiment:

$$V_c P_c = V_{c+a} P_{c+a} \xrightarrow{V_{c+a} = V_c + V_a} V_c = \frac{V_a}{\frac{P_c}{P_{c+a}} - 1} \tag{2.9}$$

Where P_c is the initial pressure in V_c, V_{c+a} is the combined volume of V_c and V_a, and P_{c+a} is the pressure when gas expands from V_c into V_a (which is under vacuum before gas expansion). P_c and P_{c+a} are measured with the pressure sensor. V_a is known because it was pre-determined by using calibration volumes and Boyle's law. The volumes of V_a and V_c are 0.6 mL and 3.0-7.0 mL, respectively, and should ideally be kept as small as possible to ensure the evolving gases are not diluted to the extent that they are under the detection limit for the MS and pressure sensor.

The final OEMS-specific preparation step to consider is that the electrochemical gas cell needs an extended equilibration/open circuit voltage (OCV) time ($\sim$5 hours) after connection to the OEMS instrument but before the experiment is initiated to achieve two things. First, a stable temperature must be reached for reliable pressure monitoring during the experiment. Second, OEMS gas sampling is conducted during the equilibration time to achieve a stable solvent background in V_c and V_a before the OEMS experiment. Otherwise, confusing ion current trends will be detected because of a shifting solvent baseline at the start of the OEMS experiment.

Beyond the preparatory steps are general factors influencing the OEMS results, which cannot be avoided but should be considered when analysing OEMS data. First, the OEMS instrument samples gas at discrete intervals, which does not account for the onset of gassing reactions, potentially affecting gas homogeneity in the headspace at each measurement point, which contributes to an offset between the total pressure changes and the sum of partial pressures. Still, gas diffusion (equation 2.6) is fast enough when using a 10-minute sample interval that it can be assumed that gas heterogeneity from a single gas evolution reaction only affects the subsequent measurement point before the gas has diffused homogeneously throughout the headspace.

Gas concentrations can be measured down to the single ppm range on the custom-made OEMS. However, qualitative trends are possible to discern at even lower gas concentrations, enabling the detection of gas from reactions on a minuscule level. Still, many commercial quadrupole mass spectrometers similar to what is used in this thesis work claim sensitivities good enough to quantify gas concentrations down to the ppb range. The reduced sensitivity of the OEMS compared to the listed sensitivity values stems from various factors. Volatile electrolyte species such as linear carbonates or ethers im-
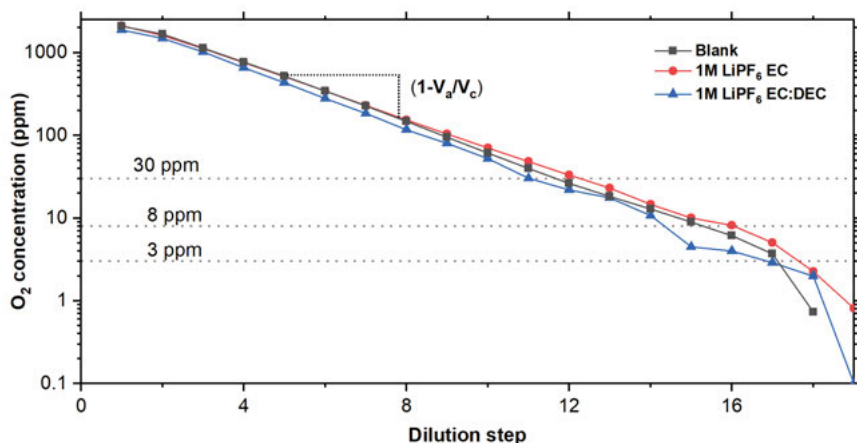
Figure 2.6. Dilution of O_2 in different mediums for OEMS quantification sensitivity limit.

pact measurement sensitivity, as a significant portion of the extracted gas from the electrochemical gas cell comprises the solvent compared to gases evolved from the studied system. These solvents' mass spectra often overlap with the m/z channels dedicated to tracking target gases, reducing the S/N ratio by raising the ion current background. Additionally, the volatile solvent concentration can decrease throughout an extended OEMS measurement, complicating the assignment of a fixed $\bar{S}$ value to accommodate the electrolyte background. How different electrolytes affect the quantification was determined in **Paper I** and is shown in Figure 2.6. The electrochemical gas cell was filled with 2000 ppm O_2 in Ar calibration gas with a glass fibre separator soaked in different electrolytes. Measurement points were taken every 10 min, and the electrochemical gas cell gas was diluted with pure Ar for each step, yielding a dilution trendline. The slope of the blank cell trendline equals $1 - V_a/V_c$ down to 3 ppm. As LiPF$_6$ EC is added to the cell a clear deviation is reached at 8 ppm, and when the more volatile DEC is added to the electrolyte, deviations are introduced already at 30 ppm.

Gas solubility in the electrolyte according to Henry's law needs to be considered as it can affect the gas composition in the headspace. The effect is demonstrated with CO_2 and EC:DEC solvent in Figure 2.7 (from **Paper V**), as different electrolyte volumes lead to noticeable changes in the OEMS measurements. The electrolyte volume was changed from 50 to 100 to 200 and finally to 400 μL in GC | 1 M LiPF$_6$ EC:DEC | LFP cells, which shifted the onset for CO_2 evolution from 2.5 V vs. Li$^+$/Li for 50 μL to 1.7 V vs. Li$^+$/Li for 400 μL. Additionally, the initial CO_2 evolving process was undetected for electrolyte volumes $\geq$ 200 μL, and is only clearly discerned in the 50 μL electrolyte cell. Therefore, the electrolyte volume should be carefully considered

and minimised before running OEMS experiments to ensure no process goes undetected.

Further complexity is added to the data analysis when gas from both the negative and positive electrodes are mixed in the headspace. To prevent the mixing of gases, two approaches are available. The use of a two-compartment cell, which incorporates a Li-conducting glass separator between the electrodes [82], seals the electrodes from each other and gases only from one electrode are detected. Alternatively, employing a counter electrode that operates within a potential range stable for the electrolyte can be effective. Importantly, the electrode itself should neither release gas at any lithiation degree nor when it decomposes. An example electrode active material fulfilling these requirements is $LiFePO_4$ (LFP).

Another important aspect to consider is that multiple reactions that generate the same gas can occur simultaneously, which complicates assigning gas evolution to specific reactions. Additionally, when gas evolution and consumption occur concurrently, it becomes impossible to determine the extent of each reaction. This is because only the net difference between the two processes is measurable, not the individual contributions.

Finally, the detected gases in OEMS are generally not the products of interest, *e.g.* C_2H_4 is the byproduct from EC reduction and the SEI products are what are interesting. In other words, direct detection of liquid or solid products cannot be achieved with OEMS as the sole analytical technique. Still, likely reaction products and pathways can be constructed via deduction, but to achieve a full understanding of the LIB chemistry, complementary analysis is needed.
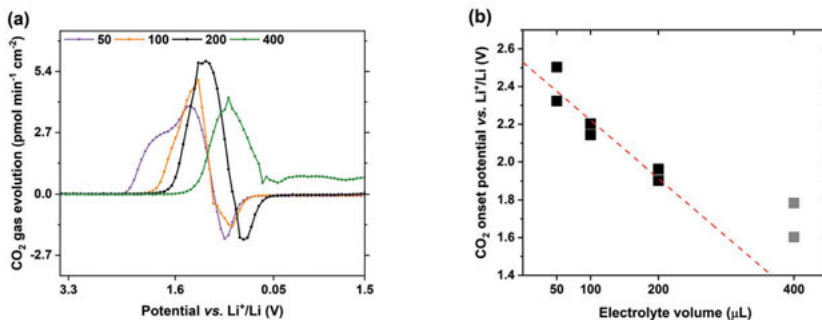

Figure 2.7. The CO_2 evolution onset vs. electrolyte volume in GC | 50 – 400 μL 1 M $LiPF_6$ EC:DEC | LFP cells. a) The CO_2 gas evolution trends depending on electrolyte volume. b) The detected onset for cells with varying electrolyte volumes. Every data point represents a separate experiment. The dashed red line shows the trend for CO_2 onset vs. electrolyte volume. The cells at 400 μL do not follow the trend as other CO_2 evolving processes likely have been triggered at this point.

2.3 Complementary techniques

2.3.1 Electrochemical Quartz Crystal Balance

Electrochemical Quartz Crystal Microbalance (EQCM) is an analytical technique that combines the principles of quartz crystal microbalance (QCM) with electrochemistry. QCM operates based on the piezoelectric properties of quartz crystals. By applying an oscillating electric field and tracking the resonance frequency of the quartz crystal, changes on the quartz surface and the medium in its closest vicinity can be monitored. For EQCM measurements, the quartz crystal is coated with a conductive layer, usually a noble metal, such as gold (Au). The conductive layer is then utilised as an electrode in an electrochemical cell simultaneously as the resonance frequency is analysed.

Two theoretical models are commonly employed in EQCM data analysis: the Sauerbrey and Voigt models. The Sauerbrey model relates the frequency change to the mass change linearly and is valid for thin and rigid films [83]. The Sauerbrey model becomes inadequate when dealing with softer or more viscoelastic layers. Here, the Voigt model comes into play [84, 85]. The Voigt model accounts for both the mass and viscoelastic properties of the film by fitting the shifts in both frequency and dissipation. It provides a more comprehensive understanding of the mass change and mechanical properties of the layer deposited on the electrode surface.

2.3.2 *Operando* vibrational spectroscopy

Operando spectroscopy, specifically Infrared (IR) and Raman spectroscopy, combined with electrochemistry are powerful analytical techniques used to study electrochemical reactions, formation and consumption of reactants and products, and structural changes in materials as they occur in real-time.

IR spectroscopy operates on the principle that molecules absorb specific frequencies of infrared light that correspond to the vibrations of the bonds between atoms. In *operando* IR spectroscopy, a sample is irradiated by IR light while undergoing a reaction. The IR light interacts with the sample, and the molecules within the sample absorb specific wavelengths of the IR light, leading to a spectrum that represents the vibrational modes of the molecules. This spectrum is used to identify the chemical species present and to monitor changes in the sample composition during the reaction.

Raman spectroscopy is based on the phenomenon of Raman scattering, where photons are inelastically scattered upon interaction with a sample. Most of the light is elastically scattered, but a small fraction is inelastically scattered, which provides information about the vibrational energy levels of the molecules in the sample. Raman spectroscopy is particularly useful for studying materials that are IR inactive or have overlapping IR bands, as it offers complementary information.

3. Gas evolution in Li-ion cells at elevated temperature and high voltage

Gas evolution in a classical Li-ion cell configuration based on $LiCoO_2$ (LCO) | 1 M $LiPF_6$ EC:DEC (1:1 volume ratio) | Graphite was explored as a first test case for the OEMS developed within the thesis. Overall, the LCO | Graphite system, when optimised, can achieve close to 100% coulombic efficiency during operation. However, side processes can be expected, at both the negative and positive electrodes, especially when the system is pushed outside of its safe voltage window during the formation cycles at elevated temperatures. An overview of the LCO | 1 M $LiPF_6$ EC:DEC | Graphite gas-evolving processes is presented in this Chapter to demonstrate gas evolution profiles in LIBs (based on **Paper I**). The LCO and Graphite electrodes were first analysed separately to distinguish what gases originate from which electrode. This was done by using a counter electrode, LFP, that does not generate any gas and has a working potential range where the electrolyte solution and residual contaminants are neither oxidised nor reduced. Gas evolving reactions are only briefly mentioned here with a citation to relevant literature, and commonly reported products are summarised in Table 3.1. A selection of gas-evolving reactions is discussed further in Chapters 4 and 5.
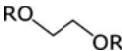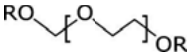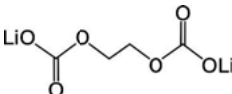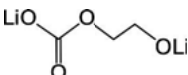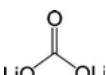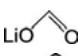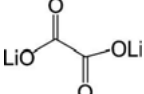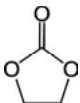
3.1 Graphite gas evolution

The current and gas evolution profiles of a Graphite | 1 M $LiPF_6$ EC:DEC | LFP cell during cyclic voltammetry (CV) at 0.1 mV/s rate from ~ 0.2 V to vertex potentials 3.45 V and 2.0 V is shown in Figure 3.1. Four different gases, POF_3, H_2, CO_2, and C_2H_4 are detected with unique gas profiles.

POF_3 is the detected volatile product from $LiPF_6$ decomposition when it reacts with either water or protons [61, 86, 87]:

$$H_2O + LiPF_6 \rightarrow 2HF + POF_3 + LiF \tag{3.1}$$

$$H^+ + PF_6^- \rightarrow HF + PF_5 \text{ (observed as } POF_3) \tag{3.2}$$
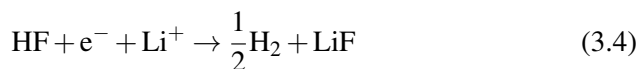
PF_5 is typically not registered in the MS as it rapidly reacts with its surrounding environment resulting in the formation for POF_3 [86]. The reaction onset for POF_3 evolution occurs at ~ 0.4 V but is not potential-dependent. Instead, the thermally activated reactions spontaneously occur at the elevated

Table 3.1. *Structures of relevant molecules in this thesis.*

Molecule	Structure
Ethylene glycol (EG) derivatives	
Poly ethylene glycol (PEG)	
Lithium ethylene dicarbonate (LEDC)	
Lithium ethylene monocarbonate (LEMC)	
Lithium carbonate (Li_2CO_3)	
Lithium formate (HCO_2Li)	
Lithium oxalate ($Li_2C_2O_4$)	
Ethylene carbonate (EC)	

cell temperature of 50 °C. The dependency of H_2O and H^+ for POF_3 evolution is evident, as indicated by a decrease in POF_3 evolution coinciding with the start of H_2 evolution at 1.0 V. The H_2 evolution stems from a few possible reaction pathways with protons involved:

$$H^+ + e^- \rightarrow \frac{1}{2}H_2 \tag{3.3}$$

$$HF + e^- + Li^+ \rightarrow \frac{1}{2}H_2 + LiF \tag{3.4}$$

$$H_2O + e^- \rightarrow \frac{1}{2}H_2 + OH^- \tag{3.5}$$

The H_2 evolution peak slowly decays throughout the cathodic sweep and into the anodic sweep. The exact source of the H_2 evolution cannot be determined from this data and is investigated further in Chapter 4 and **Paper V**.
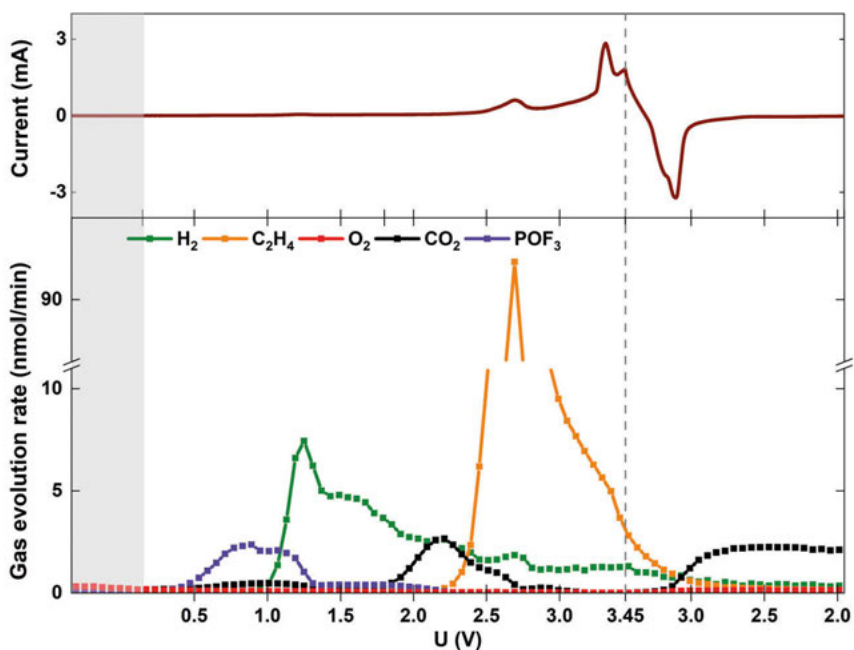
Figure 3.1. Current and gas evolution profiles for a Graphite | 1 M $LiPF_6$ EC:DEC (1:1) | LFP cell during CV at 0.1 mV/s scan rate and 50 °C. The dashed line indicates the vertex potential. The grey area corresponds to the OCV period.

The next detected gas, CO_2, evolves to a minor extent simultaneously as POF_3 starting at ∼0.5 V, which can be explained by EC hydrolysis, forming ethylene glycol (EG) derivatives[i] as the cell temperature increases [50]:

$$H_2O + EC \rightarrow CO_2 + EG \tag{3.6}$$

A temporary decrease in CO_2 evolution rate is detected at 1.0 V since proton sources are reduced via reactions 3.3-3.5. However, CO_2 evolution is observed again at ∼1.7 V. This is due to the newly formed hydroxides (resulting from reaction 3.5), which react readily with EC. This reaction leads to the formation of EG and, subsequently, poly(EG) [36, 50]:
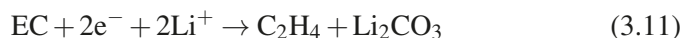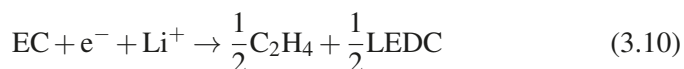
$$EC + OH^- \rightarrow CO_2 + EG \tag{3.7}$$

$$EG + EC \rightarrow CO_2 + PEG \tag{3.8}$$

---

[i]In this thesis – "EG" is used to describe not only ethylene glycol with OH end groups with a molecular net charge of zero, but species with a charge, radical or different end groups (*e.g.* Li instead of H) are possible as well.

41

CO_2 evolution decreased again at $\sim$2.2 V likely due to gas consumption reactions [36, 54]. Finally, during the anodic sweep at $\sim$3.2 V, CO_2 evolves yet again, which could be caused by CO_2 consumption reactions slowing down or stopping, but CO_2 evolution reactions continuing. The CO_2 evolution at this stage could be caused by residual contaminants (reaction 3.7) [36] or SEI decomposition [88]:

$$LEDC \rightarrow CO_2 + LEMC \tag{3.9}$$

The fourth and last detected gas, C_2H_4, reaches an order of magnitude higher gas evolution rates compared to the other evolving gases. The dominating C_2H_4 reaction onsets at $\sim$2.3 V and is due to EC reduction, forming the main part of the SEI on the graphite electrode. The EC-derived reduction products are commonly reported to be lithium ethylene dicarbonate (LEDC) and lithium carbonate (Li_2CO_3) [42, 45, 89]:

$$EC + e^- + Li^+ \rightarrow \frac{1}{2}C_2H_4 + \frac{1}{2}LEDC \tag{3.10}$$

$$EC + 2e^- + 2Li^+ \rightarrow C_2H_4 + Li_2CO_3 \tag{3.11}$$

3.2 LiCoO$_2$ gas evolution

Gases originating from LCO were investigated by studying a LCO | 1 M LiPF$_6$ EC:DEC | LFP (fully delithiated) cell during CV at 0.1 mV/s scan rate from OCV to 1.45 V ($E_{LCO} \simeq 4.95$ V[ii] vs. Li$^+$/Li) and back to -0.2 V at 50°C. Figure 3.2 shows the current response and detected gases; POF$_3$, CO_2 and O_2.

POF$_3$ evolution onsets during the OCV period when the OEMS cell is heating up to 50 °C, which is explained by reaction 3.1 and 3.2. Contrary to the Graphite cell, POF$_3$ is continuously evolving throughout the cyclic voltammogram because the protons are not consumed by any other process, *e.g.* reactions 3.3-3.5. Notably, the POF$_3$ evolution trend is changing throughout the cycle, and the individual reactions increasing the gas evolution rate cannot be deconvoluted, but are likely connected to processes generating more reactants for reactions 3.1 and 3.2, *e.g.* via HF-activated transition metal dissolution [91] or LCO decomposition.

The next gas, CO_2, also evolves during OCV but in two steps. The first step, which started even before data was recorded, can be explained by HF reacting with residual Li$_2$CO$_3$ on the electrodes:

$$2HF + Li_2CO_3 \rightarrow H_2O + 2LiF + CO_2 \tag{3.12}$$

[ii]LCO is normally not pushed above 4.2 V vs. Li$^+$/Li [90] to minimise the risk of side reactions, *i.e.* in this study the experimental conditions are set to promote these side reactions.
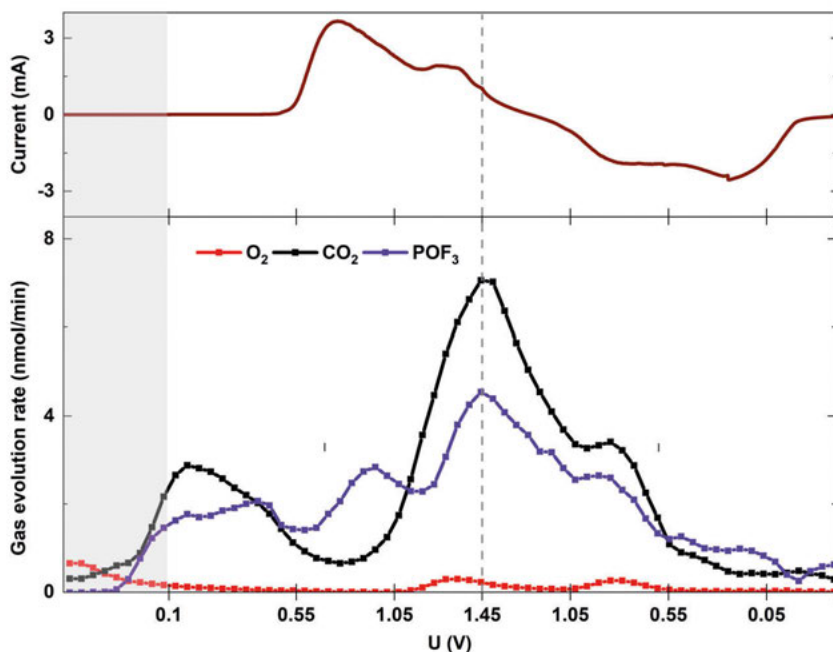
Figure 3.2. Current and gas evolution profiles for a LCO | 1 M LiPF$_6$ EC:DEC (1:1) | LFP (delith.) cell during CV at 0.1 mV/s scan rate and 50 °C. Dashed line indicate the vertex potential. The grey area corresponds to the OCV period.

The CO$_2$ evolution rate increases mid-way through the OCV period and likely corresponds to hydrolysis of EC as the cell is heating up, *i.e.* reaction 3.6. Next, CO$_2$ evolves at $\sim$0.8 V due to LCO decomposing and releasing oxygen species. The final gas, O$_2$, is the expected product to be released from the LCO structure when the lithiation degree (x) in Li$_x$CoO$_2$ goes below 0.4 [92,93], and the layered LCO decomposes into spinel and rock salt phases:

$$CoO_2 \rightarrow Co_3O_4/CoO + O^\star \qquad (3.13)$$

The O* species can subsequently recombine with another O* into O$_2$:

$$O^\star + O^\star \rightarrow O_2 \qquad (3.14)$$

However, O$_2$ evolution occurs only to a minor extent above 1.1 V. Instead, the majority of released oxygen is detected as CO$_2$ due to oxygen species' subsequent reactions with the electrolyte [94], *e.g.*:

$$EC + O^\star \rightarrow CO_2 + H^+ + RO \qquad (3.15)$$

43

Finally, simultaneous CO_2 and O_2 peaks are detected during the anodic sweep at 1.05 V, which could be caused by a LCO H2 to H3 phase transition or trapped oxygen in the LCO electrode [95].

3.3 Full cell gas evolution

The gases originating from LCO and Graphite have been deconvoluted in Chapters 3.1 and 3.2, which will facilitate the analysis of the more complex system LCO | 1 M LiPF$_6$ EC:DEC | Graphite, where gas evolution from both electrodes can be expected. In Figure 3.3 – gases originating from thermal reactions, LCO, and Graphite can be discerned when the LCO | Graphite cell voltage is pushed to 4.85 V at 50 °C. The same gases as were registered in the LCO | LFP and Graphite | LFP cells are detected, *i.e.* H_2, C_2H_4, O_2, CO_2, and POF_3. The gases are presented in the order they appear in the voltammogram.

First, CO_2 and POF_3 are generated during OCV just before the current starts flowing through the cell, and are caused by the residual Li_2CO_3 decomposition (reaction 3.12) on the cathode side, EC hydrolysis (reaction 3.6), and $LiPF_6$ decomposition (reactions 3.1 and 3.2) in the electrolyte. The gas evolution
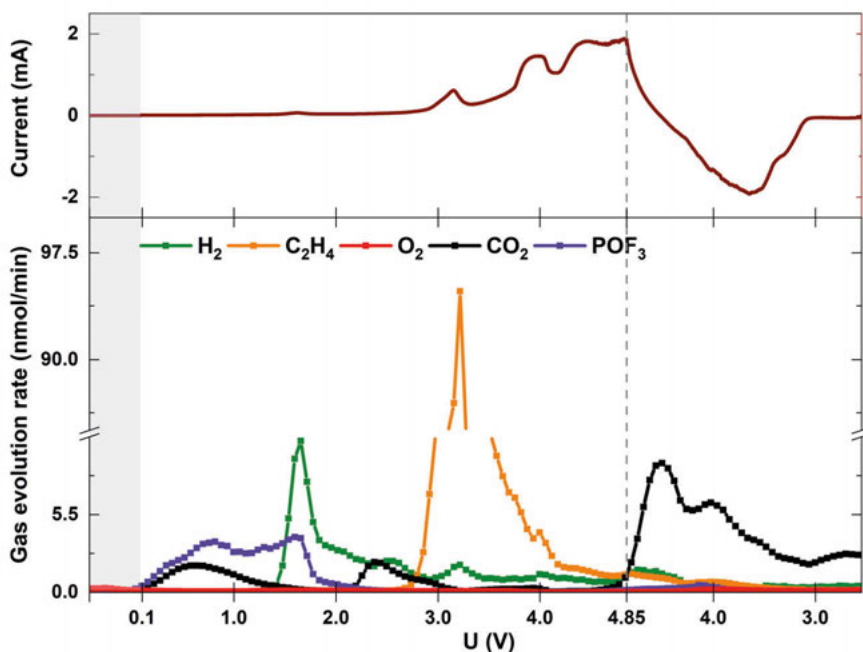

Figure 3.3. Current and gas evolution profiles for a LCO | 1 M LiPF$_6$ EC:DEC (1:1) | Graphite cell during CV at 0.1 mV/s scan rate and 50 °C. Dashed line indicate the vertex potential. The grey area corresponds to the OCV period.

rates of CO_2 and POF_3 decrease as H_2 starts evolving at $\sim$1.5 V, which is further proof that protons are the cause for continuous POF_3 evolution in the LCO | LFP cell, and not something LCO specific. The CO_2 evolution rate increases after the H_2 evolution peak at $\sim$2.2 V, which corresponds to OH^- reacting with EC (reactions 3.7 and 3.8). C_2H_4 evolve at the Graphite electrode at 2.8 V and is assigned to EC-derived SEI formation (reaction 3.10). Finally, CO_2 evolves at the vertex potential, caused by the LCO structure releasing oxygen species (reaction 3.13).

The different gas-evolving reactions in the LCO | Graphite cell are possible to assign with the analytical help gained from the LCO | LFP and Graphite | LFP cells. Still, there are some clear differences to highlight, such as the total gas evolution of each gas species. Figure 3.4 shows the total gas evolution of each detected gas for the three cells. The values are calculated over two cycles (shown in **Paper I**) by integrating the gas evolution profiles. More gas evolves in the LCO | Graphite cell compared to the LCO | LFP and Graphite | LFP cells combined. No further conclusions are drawn here due to a few reasons. The total gas evolution is not normalised in any way since the gas evolution originates from different sources, such as surface-dependent reactions, potential-dependent reactions and Li degree in the materials. Additionally, the cells were not cycled for the same length of time, which would result in a skewed comparison of the total gas evolution.

3.4 Reflections and conclusions

Paper I shows that an overview of the gas evolution in a classical Li-ion cell is possible to achieve with our custom-made OEMS. Both major and minor reactions can be monitored, separated from each other and quantified. The gas evolution reported for this LCO | Graphite system exemplifies what formation cycles can look like. H_2, C_2H_4 and CO_2 are the main evolving gases if Graphite is present, which to a large extent relates to the reduction of residual contaminants and SEI formation. POF_3 evolution is thermally activated and proceeds as long as $LiPF_6$ has access to protons in the system, which is
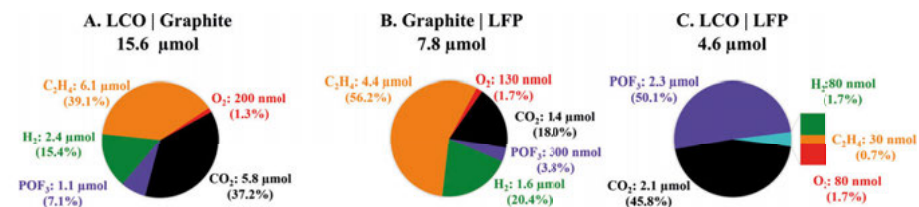

Figure 3.4. The total gas evolution over two cycles from the LCO | Graphite, Graphite | LCO and LCO | LFP cells, where the percentage of each major gas is represented in the pie charts.

the reason for the significant difference between the LCO | LFP cell and the other two cells. O_2 evolution only happens to a minor extent in the cells containing LCO, which logically would be expected from the decomposition of LCO. However, in this study, the nature of the oxygen released by LCO was not determined, but studies on similar systems have suggested that it is singlet oxygen ($^1O_2$) [96], which could react with the carbonate-based electrolyte, forming CO_2.

Still, this is not a complete picture of all possible reactions generating volatile species in a LIB cell. For example, no CO was detected in this study, which has been reported to evolve as a product of EC reduction [42,45], and is seen as a product in one of our other studies (**Paper III**). A couple of reasons for the missing CO evolution could be that CO evolves to a lesser extent at elevated temperatures and that it is challenging to separate from other evolving gases, as its mass spectrum overlaps with several other relevant gases' mass spectra. Also, deconvoluting the overlapping mass spectra is further complicated by the elevated temperature, as the solvent background is higher, compared to what it would have been at room temperature.

Finally, a comment on the choice of electrochemical cycling method for the experiment series. Normally galvanostatic charging is used for batteries,
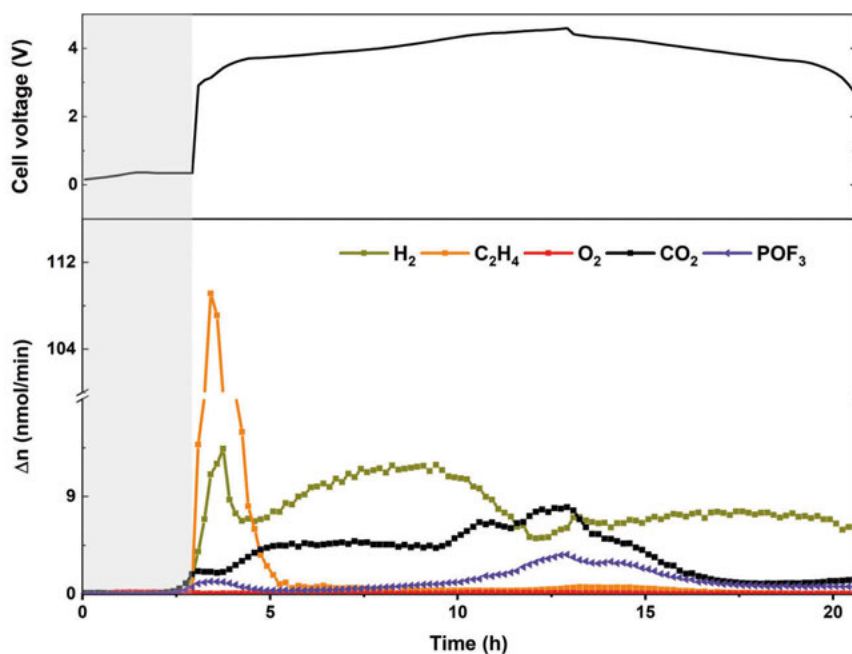

Figure 3.5. Voltage and gas evolution profiles for a LCO | 1 M LiPF$_6$ EC:DEC (1:1) | Graphite cell for constant current at C/10 rate and 50 °C. The grey area corresponds to the OCV period.

which would suppress some of the potential-dependent reactions and leave the LCO | Graphite cell at higher potentials for a longer time. However, galvanostatic cycling conditions would make it difficult to deconvolute the potential-activated gas evolution reactions as the majority of gas would evolve immediately as the constant current is applied. An identical LCO | 1 M LiPF$_6$ EC:DEC | Graphite cell to the one in Figure 3.3, but cycled with constant current is shown in Figure 3.5. Differentiating between the potential-dependent gassing reactions is nearly impossible during constant current experiments, as a wide potential range is covered within a short time frame. Depending on the goal of a study, this may of course be of interest. However, the focus of this thesis is mainly on potential-dependent reactions. Therefore, CV is the preferred cycling technique, as it simplifies separating gassing reactions from each other.

4. Negative electrode/electrolyte interphase

A complete understanding of a commercial LIB cell is nigh impossible to achieve unless every component is studied individually. The negative electrode/electrolyte interphase is one component that even though it has been studied thoroughly, remains elusive. In this Chapter, the electrochemistry taking place at the negative electrode/electrolyte interphase is explored, and factors contributing to different reaction pathways for practical and model LIB electrolytes, as well as residual contaminants are discussed. To dissect the different processes, the complexity of the LIB is reduced by using a model LIB system, and employing either a composite glassy carbon (GC) or Au electrode combined with an LFP counter electrode.

4.1 EC – the archetype electrolyte solvent

The application of EC in commercial LIB electrolytes is widespread, largely due to its effectiveness in forming an SEI, which is why it is preferred over other solvents. However, despite EC's recognised performance, the specific reaction pathways it follows to contribute to SEI formation are not completely understood. This Chapter delves into the various reactions EC undergoes, aiming to improve our understanding of this central component in LIB electrolytes.

4.1.1 Why EC is preferred: EC-PC mystery

Propylene carbonate (PC) was the favoured solvent for Li-ion electrochemistry in the mid-1900s when Li metal was the negative electrode of choice [9]. However, when carbonaceous electrodes were introduced to the field, they were incompatible with PC, leading to EC electrolytes outperforming PC in cyclability [24]. The stark difference in performance between PC and EC was surprising since the only molecular structure difference is an extra methyl group on one of the ethylene carbons for PC (Figure 4.1). This conundrum, commonly called the EC-PC mystery, still confuses electrochemists to this day. SEI stability and dissolution, solvent co-intercalation and solvent-dependent reaction pathways have been suggested as the causing problems for PC-based electrolytes when used together with a carbonaceous electrode [97–99].

In **Paper II**, the difference in performance for EC and PC was linked to the SEI stability. Direct reduction of EC and PC is well established to occur <0.9

Figure 4.1. EC (left) and PC (right) structures.

V vs. Li^+/Li and can be identified by the volatile products ethylene (C_2H_4) and propylene (C_3H_6), respectively [53, 100]. In Figure 4.2, two nominally identical GC | LFP cells were galvanostatically charged in either 1 M $LiPF_6$ EC:DEC (1:1 vol%) or 1 M $LiPF_6$ PC electrolyte solutions. In the OEMS experiment – the PC-based cell reached a potential plateau at 0.8 V vs. Li^+/Li where C_3H_6 continuously evolved, which indicates that either no SEI is deposited or if an SEI layer forms it cannot separate the electrode and electrolyte from each other, leading to continuous decomposition of PC. After ca. 1 h, a temporary electronically isolating state was reached and the potential continued below 0.8 V vs. Li^+/Li. EC reduction occurs at 0.8 V vs. Li^+/Li as well, determined by C_2H_4 evolution onset potential. However, the cell never reached a plateau, but instead continued down below 0.8 V vs. Li^+/Li immediately, a clear indication of a successful passivisation of the carbon surface. The total C_3H_6 gas evolution was found to be an order of magnitude larger than C_2H_4 evolution. Other processes potentially forming an SEI, such as residual HF and H_2O reduction were present to similar extents in both cells (by comparing the H_2 and CO_2 trends) and are therefore assumed to play a similar negligible role in the EC-PC comparison.

EQCM verified that the extensive C_3H_6 evolution in the PC cell was caused by a non-passivating and dissolving SEI layer (Figure 4.2). The mass of the EQCM carbon sensor electrode increased continuously during polarisation, indicating that deposited SEI continued to grow in thickness. A similar potential plateau as in the OEMS experiment is present for the PC cell during the EQCM measurement. As a result, the EC-based cell reaches the cut-off potential hours before the PC-based cell. After polarisation when the cells were again left at OCV, the EC-based SEI stays stable, with a slight increase in mass over time. The PC-based cell on the other hand loses most of the deposited SEI within a few hours, leaving only an incomplete SEI from residual contaminants.

The extensive PC decomposition and accompanied C_3H_6 gas evolution are caused by the high solubility and poor passivisation of PC-based SEI. In contrast, the EC-based SEI is kinetically stable and no further EC is reduced when the initial SEI forms. As a result, EC outshines PC electrolytes when combined with carbon electrodes.
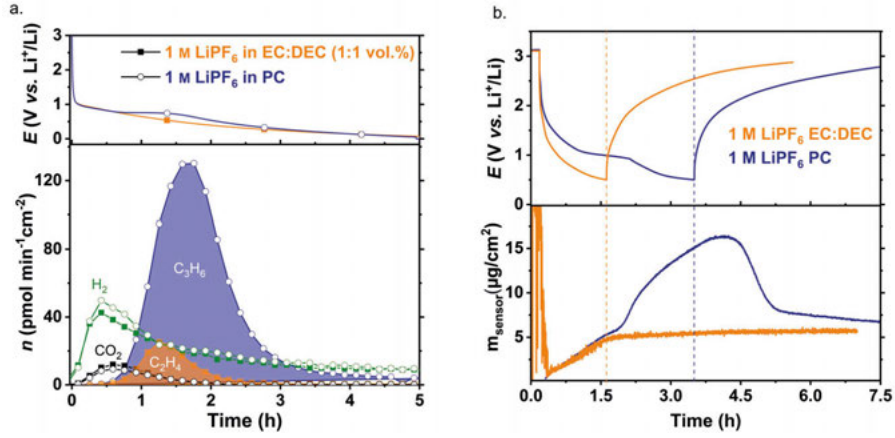
Figure 4.2. Operando investigation of EC- and PC-based electrolytes. a) OEMS experiment showcasing differences in gas evolution rates. b) EQCM experiment showcasing the mass change in EC- and PC-based electrolytes. The Voigt model fails for EC-based electrolytes up until 0.4 h due to insufficient mass deposition. Dashed lines represent when cells hit cut-off voltages and enter OCV.

4.1.2 EC reduction

The main reaction EC is known to undergo on carbon electrodes in LIBs is reduction below 0.8 V vs. Li$^+$/Li. In **Paper III**, reduction reaction pathways of EC were investigated on a GC electrode with OEMS. Figure 4.3 shows the cyclic voltammogram and gas evolution profiles of a series of GC | 0.2 M LiClO$_4$ 1,2-dimethoxyethane (DME):EC | LFP (delith. to 90% state of charge, SOC^i) cells, where the added mols of EC (n_{EC} = nmol$_{EC}$cm$_{GC}^{-2}$) is varied between 0 to 1560 nmol$_{EC}$cm$_{GC}^{-2}$. The gases evolving from EC reduction, C$_2$H$_4$ [43, 53] and CO [42, 45, 51] were tracked to distinguish any trends relating to n_{EC}. The commonly suggested EC reduction reactions are:

$$EC + Li^+ + e^- \xrightarrow{x2} LEDC + C_2H_4 \qquad (4.1)$$

$$EC + 2Li^+ + 2e^- \rightarrow Li_2CO_3 + C_2H_4 \qquad (4.2)$$
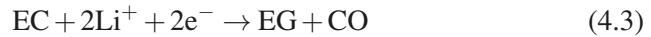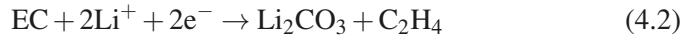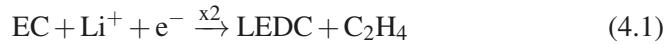
$$EC + 2Li^+ + 2e^- \rightarrow EG + CO \qquad (4.3)$$

Figure 4.3a displays the electrochemical response during the first cycle, showing consistent current profiles across all cells with different n_{EC}. A distinct peak at 1.6 V vs. Li$^+$/Li, signifying the reduction of water impurities, is the first detected electrochemical reaction. As the potential drops below 1.2 V

---

^{i}SOC is the remaining charge in an electrode material as a percentage of its total capacity.
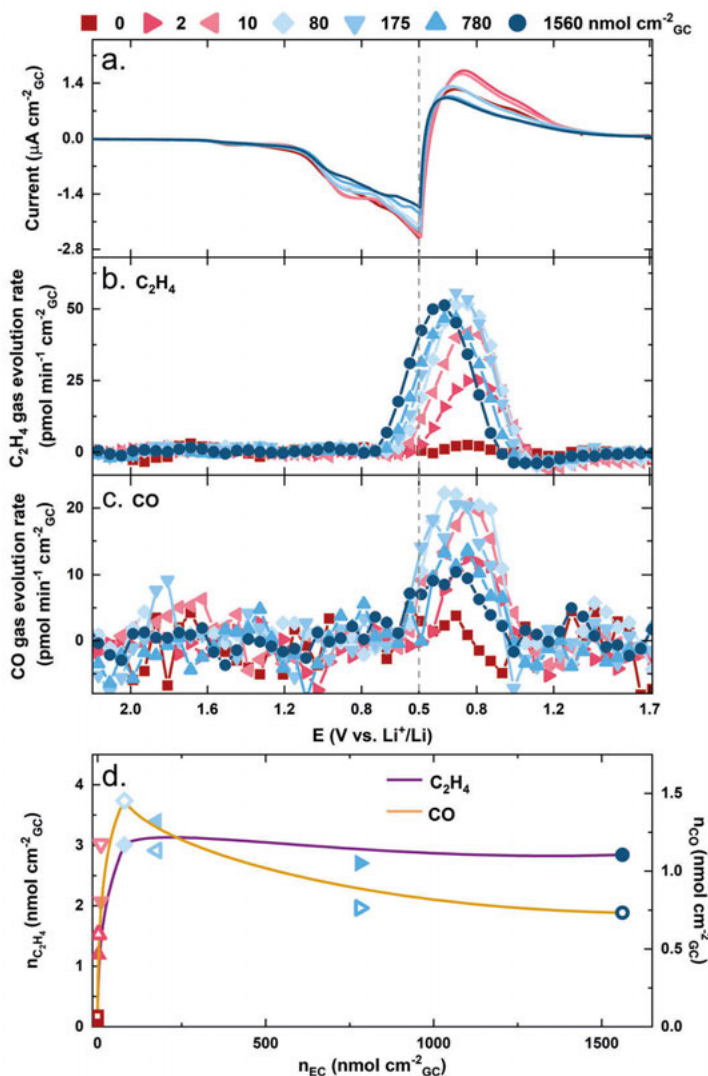
Figure 4.3. OEMS data for a GC | 0.2 M LiClO$_4$ DME:EC | LFP (delith. to 90% SOC) system cycled with CV at 0.1 mV/s rate. The grey vertical dashed line represents the vertex potential. The legend corresponds to the added n_{EC} (nmol$_{EC}$cm$_{GC}^{-2}$) in each cell. a) The current profiles for the initial cycle. b) The C$_2$H$_4$ gas evolution trend from EC reduction in the initial cycle. c) The CO gas evolution trend from EC reduction in the initial cycle. d) The total C$_2$H$_4$ (closed markers) and CO (open markers) evolution for different n_{EC}. A bezier line for C$_2$H$_4$ (purple) and CO (yellow) is used to highlight the trends.

vs. Li$^+$/Li, an increase in current is observed, primarily due to the reversible adsorption of Li$^+$ ions [101]. Below 0.8 V vs. Li$^+$/Li, currents related to the

reduction of EC are detected. Notably, higher n_{EC} in the cell correlates with decreased reversible charge, suggesting Li$^+$ loss and increased cell resistance.

C_2H_4 evolution is detected below 0.8 V vs. Li$^+$/Li in all EC-containing cells. The maximum recorded amount of C_2H_4 is $\sim$3 nmolcm$_{GC}^{-2}$ for cells with n_{EC} of 80 nmol$_{EC}$cm$_{GC}^{-2}$ or higher (as shown in Figure 4.3b and d). This indicates a fixed amount of EC is required for effective passivation of the GC surface. Below 80 nmol$_{EC}$cm$_{GC}^{-2}$, C_2H_4 gas evolution decreases, suggesting insufficient EC for a complete SEI formation process. The onset of C_2H_4 evolution shifts from $\sim$0.5 V vs. Li$^+$/Li to above 0.7 V vs. Li$^+$/Li with increasing n_{EC}, likely due to EC concentration-dependent reaction pathways and limited EC mass transport to the electrode surface at lower n_{EC}. Although it is challenging to distinguish LEDC and Li_2CO_3 reaction pathways, the significant shift in C_2H_4 onset with increasing n_{EC} suggests that the LEDC formation pathway is more prevalent due to its higher n_{EC} dependence.

CO evolution, in contrast, consistently begins at $\sim$0.6 V vs. Li$^+$/Li for all n_{EC}. The total amount of CO evolved displays a different trend compared to C_2H_4 (Figure 4.3d), indicating different kinetic processes behind these gas evolution reaction pathways. For instance, cells with $\sim$3 nmol$_{C_2H_4}$cm$_{GC}^{-2}$ show increased CO evolution as n_{EC} decreases. However, the CO evolving EC reaction pathway, likely forming EG seems less efficient in SEI stabilisation compared to the C_2H_4 evolving reaction pathways as indicated by the consistent detection of $\sim$3 nmol$_{C_2H_4}$cm$_{GC}^{-2}$ no matter the amount of CO evolution.

4.2 Early interphase processes, EC side reactions and residual contaminants

An important step towards a fundamental understanding of LIBs is to have control over the studied system. As was shown in Chapter 3 – many of the reactions detected with OEMS originate from side reactions, and they are to a large extent potential-dependent, or at least potential-triggered before propagating as a chemical reaction. A better understanding of the LIB system can be achieved by tuning the concentrations of side reaction reactants in a model system, *e.g.* via deliberate addition of contaminations. The early interphase processes were studied in **Papers IV and V**, where the build-up of the electric double layer is tracked together with the influence of residual contaminants on a gold and carbon negative electrode during formation cycles.

4.2.1 Gold surface

In **Paper IV**, an Au | 1 M LiPF$_6$ EC:DEC | LFP system was studied with *operando* Surface-Enhanced Raman Spectroscopy (SERS), OEMS and EQCM (Figure 4.4). During the SERS experiment (Figure 4.4a), the potential was

stepped 0.1 V at a time from 3.0 V vs. Li^+/Li to 0.5 V vs. Li^+/Li. The Li^+ coordinated EC band increases until ~2.3 V, indicating that the double layer and Li^+ concentration increase at the negatively charged gold surface for every potential step. The uncoordinated EC band on the other hand is not affected in the same potential range. Below 2.3 V, both the Li^+-coordinated and uncoordinated EC bands start decreasing, which is caused by residual contaminants forming an SEI, blocking the EC species from the gold surface. Still, the SEI build-up is slow and does not fully cover the Au electrode since the EC bands in the SERS experiment are not completely suppressed immediately. Further evidence for the early onset SEI at ~2.3 V vs. Li^+/Li is provided by OEMS and EQCM in Figure 4.4b and c, respectively. A H_2 evolution peak onsets at 2.5 V vs. Li^+/Li and clear mass build-up on the EQCM sensor at 2.3 V vs. Li^+/Li corresponds to HF reduction (reaction 3.4) and LiF formation. A continuous mass increase is detected until the vertex potential in the EQCM data, which agrees with the SERS data. At 1.9 V vs. Li^+/Li , H_2O reduction sets in (reaction 3.5), which OEMS and SERS combined indicate forms Li_2CO_3, *e.g.* via:

$$OH^- + CO_2 \rightarrow HCO_3^- \qquad (4.4)$$

$$HCO_3^- + e^- + 2Li^+ \rightarrow Li_2CO_3 + \frac{1}{2}H_2 \qquad (4.5)$$
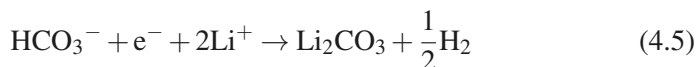
The final H_2 evolving peak onsets at 1.0 V vs. Li^+/Li, but could not be determined in this study, as no complementary results were garnered from the other *operando* measurements.

Finally, in the OEMS data, C_2H_4 and CO_2 are detected at 2.2 V vs. Li^+/Li and 1.9 V vs. Li^+/Li, respectively. C_2H_4 could correspond to EC reduction (reaction 3.10) as the overpotential for the reaction differs for carbon and gold surfaces. CO_2 on the other hand is caused by EC ring-opening reaction as the subsequent reaction to H_2O reduction (reaction 3.7).

4.2.2 Carbon surface

Five nominally identical GC | 1 M $LiPF_6$ EC:DEC | LFP cells were investigated with OEMS in **Paper V**. The Baseline cell was assembled immediately after the GC electrode was dried. The Delayed cell had the GC electrode stored in an inert Ar environment for two weeks after drying and before assembly. The cont0, -48 and -96 cells had 300 ppm H_2O added to the electrolyte at different times before cell assembly. The cell differences are summarised in Table 4.1. The focus of the study was to determine the possible reaction pathways EC undergoes beyond reduction, *e.g.* ring-opening, and how it influences the SEI on a carbon surface. EC ring-opening refers to the chemical reaction between EC and possible initiators, such as OH^- (reaction 3.7), where the
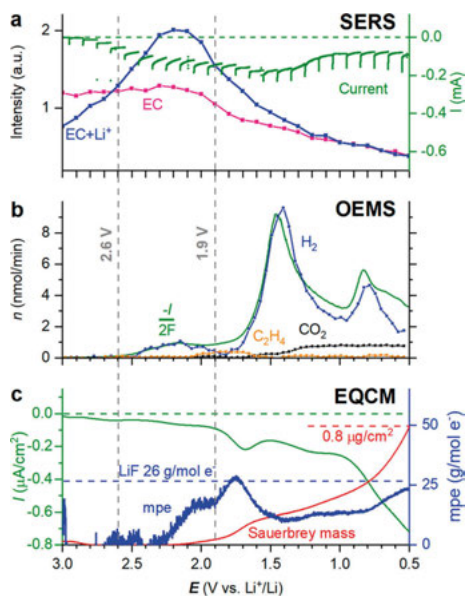
Figure 4.4. Operando investigation of an Au | 1 M LiPF$_6$ EC:DEC | LFP system. a) SERS data with fitted intensities of the Li$^+$-coordinated and uncoordinated EC bands, and the current profile during potentiostatic steps. b) OEMS data with faradaic current ($\frac{-I}{2F}$), and H$_2$, C$_2$H$_4$ and CO$_2$ evolution rates during the reductive sweep. c) EQCM data with current density, mass change, and mass change per mole of electrons transferred (mpe) as a function of applied potential.

extent of the reaction can be manipulated for example by adding H$_2$O to the electrolyte.

The current responses and gas evolution rates of H$_2$, CO$_2$, and C$_2$H$_4$ are shown in Figure 4.5. The gases shown were selected because the reaction pathways of interest could be tracked via the different gases, EC reduction – C$_2$H$_4$, EC ring-opening – CO$_2$, and HF and H$_2$O reduction – H$_2$. All cells exhibit similar currents, with minor variations at the vertex potential 0.5 V

Table 4.1. *Cell composition differences for cells presented in Figure 4.5. The electrode age column shows how long GC electrodes were stored in an inert Ar atmosphere before cell assembly. The timing (h) column shows how many hours before cell assembly H$_2$O was added to the electrolytes.*

	Electrode age (days)	H$_2$O added (ppm)	Timing (h)
Baseline	0	0	-
Delayed	14	0	-
Cont0	0	300	0
Cont48	2	300	48
Cont96	4	300	96

vs. Li^+/Li. In the first cycle, the majority of the electrode charge is reversible Li^+ ion de-/adsorption on the GC surface [101]. Irreversible electrochemical reactions are observed at ~1.2 V vs. Li^+/Li and ~0.8 V vs. Li^+/Li for all cells, and the Cont48 and -96 cells have an additional current peak at ~2.2 V vs. Li^+/Li, contrary to the other cells, which is caused by HF reduction (reaction 3.4).

The onset potential for H_2 evolution in the Baseline, Delayed and Cont0 cells is 1.6 V vs. Li^+/Li, suggesting that H_2 primarily stems from water impurity reduction (reaction 3.5), and the magnitude of gas evolution rate increases according to Delayed<Baseline<Cont0. The clear difference between Cont0 and the other cells is expected. However, the difference between Baseline and Delayed is more surprising but can be explained by the GC surface drying during the inert Ar storage. The surface groups on carbon electrodes have been shown to play a significant role in electrolyte reduction and SEI formation in LIBs [102, 103]. In this study, we hypothesise that the surface group composition changes over time despite the 12-hour vacuum and heat treatment of all electrodes when introduced into the inert atmosphere of the glovebox, resulting in the stark gas evolution difference between Baseline and Delayed cells. The Cont48 and -96 cells have a separate H_2 peak above 2.0 V vs. Li^+/Li, which is due to HF reduction, and a decreasing H_2 trend is present below 1.6 V vs. Li^+/Li as water is consumed to form HF in the electrolyte over time [104].

At least three distinct H_2 evolution peaks are observed below 1.6 V vs. Li^+/Li. The first H_2 peak is directly tied to water reduction. However, the peaks following are more difficult to deconvolute as they could either be caused by a temporary suppression of H_2O reduction, a temporary proton-consuming reaction, or the onset of a new reaction producing H_2. Evidence for a different proton source is shown in Chapter 5.1 when additives are introduced to the model system.

Next, the EC reduction pathway is favoured when the GC surface is dried out during extended storage in an inert Ar atmosphere, as is seen by the increased C_2H_4 evolution in the Delayed cell compared to the Baseline cell. On the other hand, the addition of H_2O decreases the C_2H_4 evolution to a similar extent for the Cont0, -48, and -96 cells compared to the Baseline cell. Interestingly, the EC reduction reaction is affected similarly if the residual contaminants are dominated by H_2O or HF, and only the added amount of residual contaminants affects the EC reduction reaction pathway.

Finally, the CO_2 gas evolution correlates to H_2, since both begin at ~1.7 V vs. Li^+/Li in the Baseline, Delayed and Cont0 cells, and increase according to the same trend, *i.e.* the H_2O content clearly increases CO_2 gas evolution, and extended GC electrode storage time in inert Ar atmosphere decreases the CO_2 evolution. An additional CO_2 evolution reaction was found to start already at 2.5 V vs. Li^+/Li (see Figure 2.7), which we hypothesise originates from oxygenic surface groups on the GC electrode participating in ring-opening of
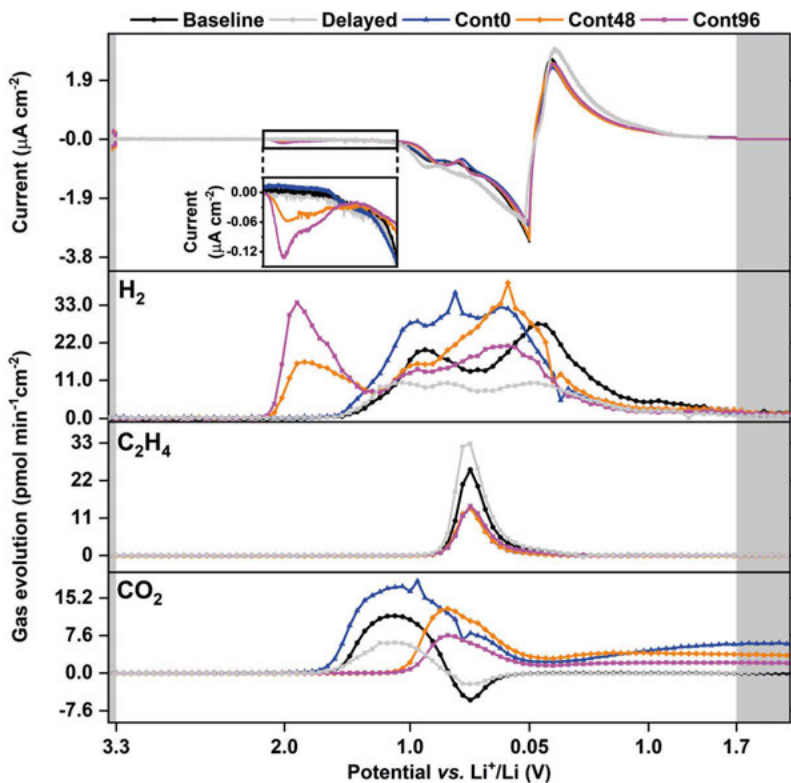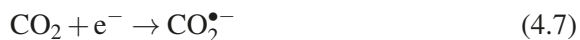
Figure 4.5. Current and gas evolution profiles for five nominally identical GC | 1 M LiPF$_6$ EC:DEC | LFP cells during CV at 0.1 mV/s rate. The differences between the cells are listed in Table 4.1.

EC. However, the CO_2 evolving reaction at 2.5 V vs. Li$^+$/Li was only detected at low electrolyte volumes, likely due to the high solubility of CO_2 in the electrolyte, which leads to insufficient CO_2 concentration in the headspace to be detected by the MS at larger electrolyte volumes. The Cont48 and -96 cells do not follow the same CO_2 trends as the other cells and are not as clearly connected to H$_2$ evolution. Instead, the CO_2 evolution onset is shifted to lower potentials ($\sim$1.0 V vs. Li$^+$/Li). For the Baseline, Delayed and Cont0 cells, a decrease in the CO_2 evolution occurs at $\sim$1.0 V vs. Li$^+$/Li, which may correspond to CO_2 consumption reactions previously proposed in literature [54]:

$$CO_2 + OH^- + 2Li^+ \rightarrow Li_2CO_3 + H^+ \tag{4.6}$$

$$CO_2 + e^- \rightarrow CO_2^{\bullet -} \tag{4.7}$$

$$CO_2^{\bullet -} + 2Li^+ \rightarrow Li_2C_2O_4 \tag{4.8}$$

56

$$\text{CO}_2^{\bullet -} + \text{Li}^+ + \text{H}^+ + \text{e}^- \rightarrow \text{HCO}_2\text{Li} \qquad (4.9)$$

The extent of the CO_2 consumption reaction is not possible to extract from these experiments since consumption and evolution occur simultaneously and only the difference between the two is detected by the MS. The importance of CO_2 for the SEI formation should not be neglected, as it may be a crucial reactant for a well-functioning SEI [54]. Finally, in the three cells with H_2O added, continuous CO_2 evolution is observed during and after the anodic sweep with no sign of stopping, indicating that contaminants (for example OH^-) are left in the system, which chemically reacts with EC to produce CO_2 (reaction 3.7).

4.3 Reflections and conclusions

The final products of all reactions occurring at the negative electrode of a LIB are more than the sum of each reaction. Reactions interact and affect each other, where for example surface-covering reactions compete for the negative electrode surface area, leading to suppression of each other depending on which reaction pathway is favoured. Additionally, only a minor amount of the residual contaminants is needed to completely change the resulting gas evolution and subsequently the SEI. This, of course, complicates any attempt to elucidate the interphase reactions, and the comparison of results to other studies, since the reported parameters and actual parameters behind an observation might not be a causality but a correlation, and additional (not considered) parameters play a significant role. If general conclusions are to be drawn, the conditions of the system under study need to be understood and controlled, and therefore model systems are ideal.

The model systems Au | LFP and GC | LFP were chosen to facilitate a more straightforward analysis of the early electrode/electrolyte processes and SEI formation at the negative electrode. However, it is important to note that even within these simplified systems, a wide range of reactions occur, making a comprehensive understanding of all these reactions quite challenging. The primary focus of this study was on the reaction pathways involving the most basic components of the system, namely EC, H_2O, and HF. It is crucial to recognise, though, that these three components, while pivotal to the interphase, are not the only influencers. Other reactions also impact the interphase. For instance, $LiPF_6$ is known to produce products besides HF and LiF, such as various organophosphates, which can influence the negative interphase of LIBs [62, 105].

Still, through this work, a clearer understanding of the negative electrode interphase is gained by examining the competing reactions that form the SEI. Figure 4.6 shows the relationship between CO_2 evolving reactions (mainly residual contaminants) and C_2H_4 evolving reaction (EC reduction), where a

linear relationship appears, indicating that the two different processes affect each other. Additionally, if the $LiPF_6$ electrolyte is aged, promoting HF formation, the CO_2 and C_2H_4 trend is broken. Instead, a third parameter is introduced to the SEI formation. A simple composition diagram can be pedagogically visualised for the relationship between H_2 from HF reduction, CO_2 evolving reactions and C_2H_4 evolving reactions, where they all compete for the finite carbon surface (Figure 4.6).
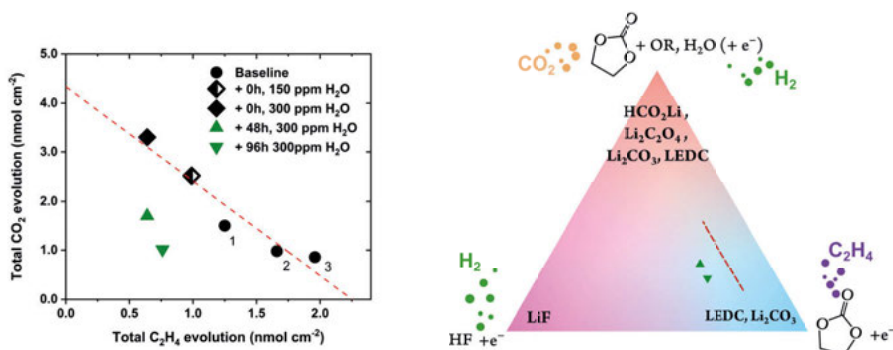
Figure 4.6. The competing nature of surface covering reactions in GC | 1 M $LiPF_6$ EC:DEC | LFP cells (90% SOC). To the left: gas evolution changes with added concentrations of H_2O (squares) or HF (green triangles) in the electrolyte. The numbered data points are identically prepared Baseline cells, but the GC electrode with a higher number has been stored for a longer duration in an inert Ar atmosphere before cell assembly. To the right: a composition diagram of the SEI formed on the GC electrode. The final composition depends on the relative concentration of HF to other residual contaminants (H_2O or surface groups) to GC surface area. The data points in the left figure are represented in the diagram (to the right) by the red dashed trendline and green triangle data points.

5. Layer-forming electrolyte additives

The negative electrode/electrolyte interphase can be designed and optimised by introducing electrolyte additives to the studied system, hence providing characteristics and functions not provided by the base electrolyte. This chapter builds on what we have learnt about the negative electrolyte interphase in Chapter 4, by investigating what aspects are affected if common additives are added to the system, namely VC and LiBOB. The additives are studied in a model system, which in its base form consists of GC | 0.2 M LiClO$_4$ DME | LFP (90% SOC). DME was selected as the primary electrolyte solvent because of its low reduction potential and high achievable purity, thereby reducing the presence of residual contaminants. LiClO$_4$ was chosen over the more commonly used LiPF$_6$ due to the latter's known reactivity with electrolyte reduction products, which could introduce additional complexity to the system.

5.1 Vinylene carbonate

VC is the most prevalent additive in LIBs (Figure 5.1), primarily due to its SEI-forming properties. VC has been reported to affect both the positive and negative electrode through layer formation, although a beneficial effect is mainly seen at the negative electrode [20, 21, 106, 107]. However, evidence for VC possessing scavenging properties was garnered in **Paper III**, when the contribution of VC at different concentrations was investigated.

Figure 5.2 displays cyclic voltammograms and the evolution patterns of CO$_2$ and H$_2$ gases for GC | 0.2 M LiClO$_4$ DME:VC:EC | LFP (90% SOC) cells with n_{VC} ranging from 0 to 1280 nmol$_{VC}$cm$_{GC}^{-2}$ and n_{EC} ranging from 0 to 145 nmol$_{EC}$cm$_{GC}^{-2}$). The first electrochemical activity onsets between 1.9 and 1.6 V vs. Li$^+$/Li in the current profile (shown in Figure 5.2a). Cells with
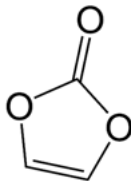

Figure 5.1. VC structure.

VC exhibit a consistent negative current trend down to ~1.4 V vs. Li$^+$/Li, while at the same time lacking a distinct plateau for H_2O reduction observed in the DME baseline cell. In cells with VC concentrations ≥ 865 nmol$_{VC}$cm$_{GC}^{-2}$, a peak at 1.4–1.3 V vs. Li$^+$/Li indicates the early formation of an SEI layer. Cells with VC concentrations ≤ 180 nmol$_{VC}$cm$_{GC}^{-2}$ do not show a distinct peak in this range. A new peak at ~0.8 V vs. Li$^+$/Li is apparent in cells with ≥ 865 nmol$_{VC}$cm$_{GC}^{-2}$, associated with CO_2 consumption reactions below 1.0 V vs. Li$^+$/Li. Similar reactions are expected in all VC-containing cells but are not detected to the same extent for ≤ 180 nmol$_{VC}$cm$_{GC}^{-2}$ cells.

CO_2 gas evolves already at potentials above 2.0 V vs. Li$^+$/Li, before the current onset at approximately 1.9 V vs. Li$^+$/Li in the cell with 1280 nmol$_{VC}$cm$_{GC}^{-2}$. However, as n_{VC} decreases, the CO_2 evolution shifts to lower potentials with reduced gas evolution rates until no CO_2 is detected in the DME baseline cell. We hypothesise that at these potentials, CO_2 may arise from VC ring-opening by surface oxygens reduced below 2.6 V vs Li$^+$/Li (similar as for EC in **Paper V**), as almost no reduction current is seen at this stage. A CO_2 consumption reaction occurs below 1.0 V vs. Li$^+$/Li, marked by a decrease in the gas evolution rate, likely related to the simultaneous consumption of surface hydrogens, forming lithium formate (reaction 4.9). The volume of CO_2 gas evolved in the initial cycle increases with n_{VC}, virtually according to a square-root behaviour. We hypothesise that this trend is explained by the reduced distance between VC molecules as n_{VC} increases, as the likelihood of the products of a ring-opened VC to react with neighbouring VCs increases with increasing n_{VC} before the reaction is terminated.

C_2H_4 gas was detected for the 5 and 70 nmol$_{VC}$cm$_{GC}^{-2}$ (and 0 nmol$_{EC}$cm$_{GC}^{-2}$) cells at ~0.6 V vs. Li$^+$/Li (Figure 5.2c). Notably, C_2H_4 is not an expected gas from VC, but from EC reduction. We hypothesise that VC can abstract reduced protons from the GC electrode surface, resulting in EC formation. The reason for only detecting C_2H_4 at low n_{VC} is that the VC-derived SEI does not cover the GC electrode completely, allowing EC access to the GC surface, and EC reduction can take place. The conversion of VC to EC in the electrolyte was also investigated with Nuclear Magnetic Resonance (NMR), and a clear EC peak was present (**Paper III**).

H_2 gas evolution starts at 1.6 V vs. Li$^+$/Li in all cells, but its rate is significantly reduced even with minimal VC presence. Two distinct H_2 evolution peaks are noted, with the second onset at about 0.7 V vs. Li$^+$/Li. The main source of H_2 evolution is H_2O and the two peaks could be a single split peak due to hydrogen consumption and lithium formate formation (reaction 4.9). Moreover, H_2 evolution is never fully suppressed at any VC concentration, and reaches a consistent plateau of 0.3 μmol H_2 at ≥ 70 nmol$_{VC}$cm$_{GC}^{-2}$, suggesting alternative H_2 sources that cannot be suppressed by VC, possibly from surface groups on the carbon.

Cells containing VC show a noticeable CO_2 evolution, unlike the EC cells in Figure 4.3, where CO_2 is below the detection limit, although identical ex-
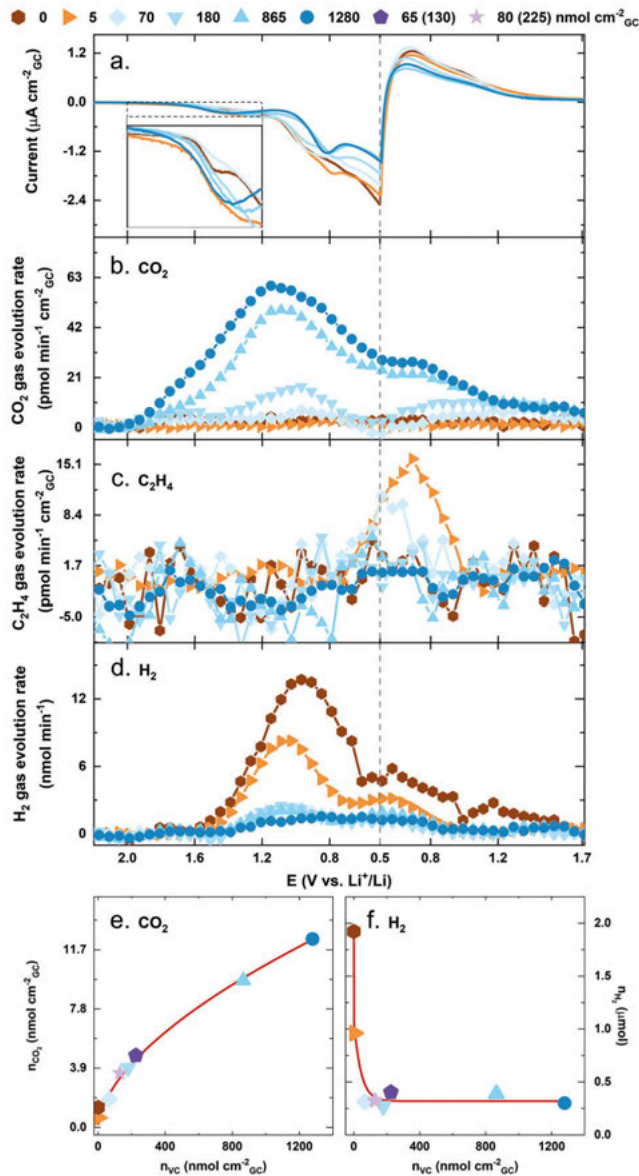
Figure 5.2. OEMS data for a series of GC | 0.2 M LiClO$_4$ DME:VC:EC | LFP (90% SOC) cells. The grey vertical line represents the vertex potential, 0.5 V vs. Li$^+$/Li. The cells denoted 65 (130) and 80 (225) are a mix of VC and EC (only shown in d and e), where the first value is n_{VC} and the value in parenthesis is n_{VC+EC}. All other cells contained no EC. a) The initial cycle voltammograms, with a zoom-in inset on above 1.2 V vs. Li$^+$/Li electrochemical profiles. b) The CO$_2$ gas evolution rates. c) The C$_2$H$_4$ gas evolution rates. d) The H$_2$ gas evolution rates. e) The total CO$_2$ evolution for different n_{VC+EC}. f) The total H$_2$ evolution for different n_{VC+EC}.

periment parameters are used for the two experiment series except for the cyclic carbonate content. Interestingly, a similar CO_2 amount is detected in cells with VC and EC mixed as in cells with only VC. This implies that the CO_2-releasing VC reaction pathway does not differentiate between EC and VC during the propagation step, allowing ring-opened VC to interact with EC in the electrolyte. This mixture of EC and VC does not affect the trend of H_2 gas evolution, since the same 0.3 μmol H_2 plateau for mixed EC and VC cells as for only VC cells is reached, indicating that the processes evolving CO_2 and H_2 are independent.

5.2 Lithium bis(oxolato)borate

The LiBOB salt (Figure 5.3) has also, just like VC, garnered attention as an additive for its promising layer-forming properties on both anode and cathode [108, 109]. One aspect of LiBOB that makes it interesting is that it forms an SEI at a high reduction potential compared to other additives. Most layer-forming additives form an SEI below the H_2O reduction potential at 1.6 V vs. Li^+/Li. LiBOB on the other hand, is reduced already at 1.8 V vs. Li^+/Li on a carbon surface and forms an SEI unaffected by H_2O reduction products. Several LiBOB reduction reaction pathways and subsequent reaction pathways have been proposed, forming Li-oxalate ($Li_2C_2O_4$) and CO_2 as reaction products, or more complex molecular combinations of oxalate borates and boron-containing semicarbonates. The reaction pathways of LiBOB, and how it influences the negative electrode interphase were investigated in **Paper VI** with OEMS, EQCM and *operando* IR.

Figure 5.4 shows the different *operando* techniques applied to investigate LiBOB reduction on a carbon surface. First, the reduction products from LiBOB in a GC | 0.2 M $LiClO_4$ DME + 50 mM LiBOB | LFP (90% SOC) cell were explored with *operando* IR during linear sweep voltammetry (LSV). The differential absorbance spectra remain unchanged until 1.8 V vs Li^+/Li, thereafter LiBOB reduction is initiated. Here, the spectral features relating to LiBOB decrease, while lithium oxalate ($Li_2C_2O_4$) features increase, indicating that LiBOB is consumed and $Li_2C_2O_4$ is formed. The LiBOB peaks slowly return to their initial intensity after the LiBOB reduction peak (below 1.5 V vs.
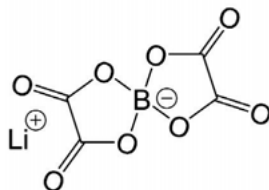

Figure 5.3. LiBOB structure.

Li$^+$/Li) as LiBOB is replenished from the bulk electrolyte. Li-oxalate on the other hand slowly increases after the LiBOB reduction peak. No significant sign of Li$_2$CO$_3$ as a reduction product from LiBOB was found in the spectra. A final unknown product following the same trends as Li$_2$C$_2$O$_4$ emerges at 1.8 V versus Li$^+$ / Li, which is assigned to the remaining oxalatoborates from the reduction of LiBOB.

The mass deposition and calculated mpe from LiBOB reduction in a carbon sensor | 0.2 M LiClO$_4$ DME + 50 mM LiBOB | LFP (ref) | LFP (90% SOC) cell were investigated with EQCM and compared to a baseline cell without LiBOB. No current peaks or notable mass deposition were observed in the absence of LiBOB. The voltammogram of the electrolyte containing LiBOB resembles that of the IR cell, with a reduction peak starting at 1.8 V vs. Li$^+$/Li, attributed to LiBOB reduction. Notably, the current observed below 1 V vs. Li$^+$/Li is lower in the LiBOB cell compared to the baseline, likely due to increased cell impedance caused by the SEI layer derived from LiBOB. The highest mass per electron (mpe) value recorded for the LiBOB electrolyte is 50 gmol^{-1}, occurring at the 1.8 V vs. Li$^+$/Li peak. This suggests the formation of Li$_2$C$_2$O$_4$, which has a mpe value of 51 gmol^{-1} (assuming a 2-electron process). Concurrently, as the reduction current increases, so does the deposited mass, which then slows down as the current diminishes. As previously noted in the IR experiment, it is unlikely that conversion of lithium oxalate occurs. Instead, other chemical reactions may be taking place, possibly involving metastable oxalatoborates and residual LiBOB salt.

Finally, a series of GC | 0.2 M LiClO$_4$ DME (+50 mM LiBOB + 5 v% EC) | LFP (90% SOC) cells were investigated with OEMS, and the predominant gases, CO$_2$, C$_2$H$_4$ and H$_2$, were tracked. The voltammograms with LiBOB present agree with IR and EQCM experiments. The introduction of EC aimed to evaluate the reactivity of LiBOB towards EC and its potential to inhibit EC reduction below 0.9 V vs. Li$^+$/Li. A notable reduction peak, starting at 1.8 V vs. Li$^+$/Li, is observed with the presence of LiBOB, accompanied by CO$_2$ evolution. The evolved CO$_2$ amount (0.85 nmol cm^{-2} for 50 mM LiBOB) is significantly lower than the consumed charge (24.3 nmol electrons cm^{-2}), showing that CO$_2$ evolution and LiBOB reduction do not have a 1:1 relationship, but instead other possible LiBOB reduction pathways presumably take place simultaneously. The LiBOB-derived SEI likely suppresses H$_2$ evolution by physically blocking H$_2$O access to the carbon surface. The evolved CO$_2$ can also scavenge protons to form Li-formate (reaction 4.9). However, the other *operando* techniques did not provide any evidence of Li-formate presence. EC on the other hand cannot suppress H$_2$ evolution to the same extent and forms CO$_2$ in low enough amounts that it goes undetected by the MS. The LiBOB SEI not only suppresses H$_2$ evolution but also EC reduction and C$_2$H$_4$ evolution are significantly suppressed. Notably, more CO$_2$ evolves when LiBOB and EC are in the same electrolyte, which could be explained by EC ring-opening reactions triggered by the reduced LiBOB products.
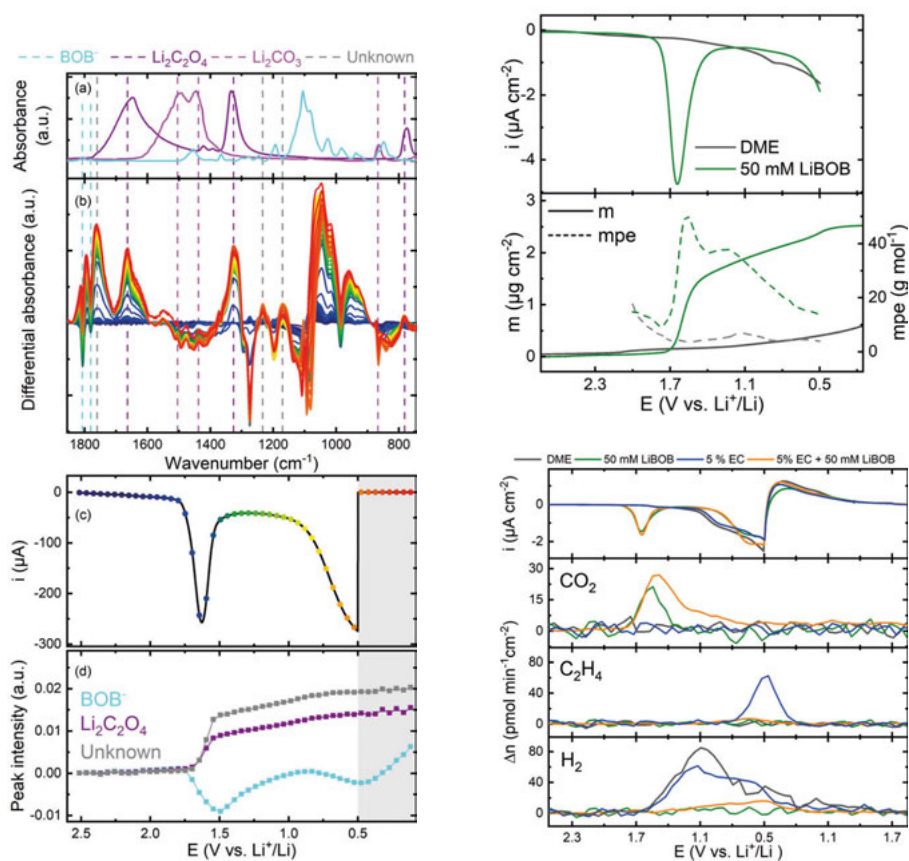
Figure 5.4. Operando investigation of LiBOB reduction. Left – *Operando* IR of a GC | 0.2 M LiClO$_4$ DME + 50mM LiBOB | LFP (90% SOC) cell with the GC electrode pressed against an attenuated total reflectance (ATR) crystal. (a) Relevant reference spectra. (b) Differential absorbance spectra between a spectrum and OCV spectrum. The data is colour-coded with the LSV data in c. (c) Current profile during CV. (d) Peak intensities of selected wavenumber throughout the CV. Top right – EQCM: The current profile together with mass deposition and mpe changes for Carbon sensor | 0.2 M LiClO$_4$ DME (+ 50 mM LiBOB) | LFP (ref) | LFP (90% SOC) cells. Bottom right – OEMS: The current and predominant gas profiles for GC | 0.2 M LiClO$_4$ DME (+ 50 mM LiBOB + 5 v% EC) | LFP (90% SOC) cells.

5.3 Reflections and Conclusions

The commonly reported benefit of the widely used VC additive is its layer-forming properties. However, the functions of VC influencing LIB cells were shown in **Paper III** to be more than forming a layer on the negative electrode. VC was shown to abstract reduced protons to form EC and generate CO$_2$ from a reaction separate from VC reduction. Additionally, we hypothesise that VC can scavenge H$_2$O directly, but more evidence is needed to draw definitive

conclusions. Interestingly, the only VC property not directly detected herein is its layer-forming capabilities. The VC-derived SEI is often claimed to be comprised of Poly(VC), but has yet to be directly detected [110]. The results derived in this thesis work cannot tell anything about the formation of poly(VC), but reopens the question about which VC properties are crucial for a well-functioning LIB.

The layer-forming property for LiBOB on the other hand was evident in **Paper VI**. The clear reduction peak of LiBOB and the simultaneous mass increase and Li-oxalate formation convincingly demonstrated that LiBOB covered the negative carbon electrode with an SEI. Still, multiple reaction pathways are possible even in a model system, exemplified by OEMS and CO_2 evolution. Additionally, the possible reaction pathways were further complicated when adding EC to the electrolyte. The LiBOB-derived SEI was proficient in blocking H_2O from reaching the negative carbon electrode surface, but the effect was worsened when EC was present and a small amount of H_2 was detected. What this tells about the SEI in a commercial cell is that multiple processes influence the SEI formation and that every combination of negative and positive electrodes, as well as electrolytes likely need a specific combination of additives to achieve high performance.

6. Conclusions

In this thesis work, a custom-made OEMS instrument was developed, validated and optimised to deepen our understanding of the side reactions in LIBs. A holistic overview of gas-evolving reactions was gained from the validation study of a classical Li-ion cell, LCO | 1 M LiPF$_6$ EC:DEC | Graphite, in **Paper I**. Three main categories of gas-evolving processes, SEI formation, side reactions with residual contaminants and structural collapse of the positive electrode were deconvoluted and quantified. Still, the study only scratched the surface of the gas-evolving processes in LIBs, and any one of the identified gas-evolving reactions could be studied further to elucidate the reaction pathways and kinetics for the relevant species.

A focus throughout this thesis work has been EC, the archetype electrolyte solvent, and its reaction pathways affecting the negative electrode in LIBs. The reason why EC is preferred in LIBs over the historically more popular PC was further investigated in **Paper II**, and was determined to be related to prevalent SEI dissolution in PC-based systems, but not in EC-based systems. The main SEI formation reaction in EC-based electrolytes, EC reduction, was investigated in **Paper III**, and it was concluded that EC undergoes decomposition reactions leading to unnecessary Li$^+$ loss, which should be avoided to achieve well-performing LIBs.

The side reactions and early interphase processes for the 1 M LiPF$_6$ EC:DEC electrolyte on a gold and carbon surface were studied in **Papers IV** and **V**, respectively. Side reactions between EC and H$_2$O residual contaminants were shown to contribute to the SEI and compete with EC reduction for the negative electrode surface. The introduction of HF to the electrolyte broke the linear relationship of the two EC reaction pathways, as a third surface-covering reaction had to be accounted for. The SEI formed from EC-based electrolytes was found to be influenced by a complex interplay of reactions since these reactions compete for the negative electrode surface and mutually suppress one another. Furthermore, even slight variations in the concentration of residual contaminants markedly affected the SEI formation.

Electrolyte additives are commonly employed to improve or complement performance requirements that EC cannot achieve. The influence of additives on the LIB formation cycles was studied in **Papers III and VI**, focusing on VC and LiBOB, respectively. VC is a frequently used additive in LIBs due to its ability to form a well-functioning SEI. However, the ability of VC to act as a scavenger of harmful species is normally disregarded but was shown to have a major influence on the gas evolution in LIBs. H$_2$ gas evolution

66

was suppressed via proton abstraction, H_2O scavenging, and the generation of CO_2, which subsequently scavenged protons as well. LiBOB on the other hand was shown to form an SEI through electrochemical reduction of BOB^- at 1.8 V vs Li^+/Li, blocking H_2O and EC from reaching the negative carbon electrode surface.

The studied systems in this thesis are all already well-established in the LIB research field. However, even though they have been studied for a few decades, the only consensus the research field has reached is that they work. There remains a significant gap in our understanding of how they work, and *operando* techniques, particularly OEMS, serve as indispensable tools for unravelling the governing mechanisms. This thesis contributes to the joint global research efforts towards a comprehensive understanding of **how** Li-ion batteries function.

7. Populärvetenskaplig sammanfattning

Dagens samhälle är beroende av energi för att fungera. Tyvärr bidrar de fossila energikällor vi idag förlitar oss på till klimatförändringen, vilket gör vår planet mindre beboelig. Det är därför viktigt att vi snabbt övergår till förnybara energikällor, såsom sol- och vindkraft. Dessa energikällor producerar dock energi periodvis och kräver därför innovativa tekniska lösningar, till exempel elektrisk energilagring, för att säkerställa energitillgången dygnet runt. I detta sammanhang spelar batteriteknologi en nyckelroll, däribland litiumjonbatterier, tack vare deras förmåga att effektivt lagra stora mängder energi.

Ett litiumjonbatteri består förenklat av en positiv elektrod, en negativ elektrod, samt en elektrolyt som möjliggör rörelse av litiumjoner mellan elektroderna. Denna process, som är reversibel, möjliggör uppladdning och urladdning av batteriet. En utmaning med denna teknik är att batteriernas kapacitet försämras över tid, delvis på grund av nedbrytningen av elektrolyten vid den negativa elektroden. För att motverka detta problem har forskning fokuserat på utvecklingen av elektrolytlösningar som kan skapa en stabiliserande hinna på den negativa elektroden, känd som Solid Electrolyte Interphase (SEI). Denna hinna är avgörande för att förhindra ytterligare nedbrytning av elektrolyten och förlänga batteriets livslängd. Trots omfattande studier kvarstår många frågor om SEI:et.

I detta arbete har analysinstrumentet Online Electrochemical Mass Spectrometry (OEMS) utvecklats och använts för att med stor precision kunna studera gaser som bildas i batterier, vilket ger insikter om sidoreaktioner och SEI-bildningen samt hur de kan kontrolleras. I **Artikel I** presenteras OEMS uppställningen tillsammans med valideringsexperiment. Ett klassiskt litiumjonbatteri undersöktes och en övergripande bild över reaktioner som producerar gas kunde uppnås. Några relevanta reaktioner som producerade gas valdes sedan ut för att studeras i mer detalj. Först lades fokus på valet av lösningsmedel i elektrolyten. **Artikel II** handlar om varför valet av elektrolyt är vad det är i dagens batterier genom att jämföra två snarlika lösningsmedel, etylenkarbonat och propylenkarbonat samt SEI:et som de bildar. Slutsatsen var att SEI:et som bildas av propylenkarbonat löses upp väldigt snabbt, vilket i sin tur leder till fortsatt nedbrytning av elektrolyt. Etylenkarbonat har inte samma problem utan SEI:et som bildas är kvar på den negativa elektroden, vilket är en avgörande orsak varför etylenkarbonat används i litiumjonbatterier.

Nästa steg var att få en djupare förståelse för etylenkarbonaten. I **Artikel III** och **V** kartlades olika etylenkarbonatreaktioner, vilka reaktioner som påverkade SEI-bildningen samt hur de olika reaktionerna kunde undertryckas

eller främjas. Tillsats av vattenföroreningar, gedigen torkning av den negativa elektroden och koncentrationen av etylenkarbonat i elektrolyten påvisades vara viktiga faktorer som påverkade etylenkarbonatens reaktionsvägar.

Föroreningar i litiumjonbatterier kan också påverka SEI:et, vilket undersöktes i **Artikel IV** och **Artikel V**. SEI:et påverkades tydligt beroende på mängden och sorten av föroreningar i litiumjonbatteriet. Dessutom var det tydligt att molekylerna som var benägna att bilda ett SEI tävlade om den negativa elektrodens yta och undertryckte varandra.

Slutligen i **Artikel III** och **VI** undersöktes hur tillsatser i elektrolyten, såsom vinylenkarbonat och litiumbisoxalatoborat, påverkar SEI-bildningen. Bägge tillsatser bidrog till SEI:et, dels genom att bilda ett SEI, men vinylenkarbonat kunde även rensa upp litiumjonbatteriet från föroreningar.

Sammanfattningsvis har utvecklingen och tillämpningen av ett OEMS instrument möjliggjort en fördjupad förståelse för de reaktioner som bidrar till åldrandet av litiumjonbatterier. Genom detta arbete kan vi erhålla en djupare förståelse för de komplexa processerna i litiumjonbatterier, vilket är avgörande för att förbättra deras livslängd och prestanda. Denna forskning är ett framsteg i strävan efter att utveckla mer hållbara och effektiva energilagringslösningar, vilket är betydelsefullt för att snabba på omställningen till ett hållbart samhälle baserat på förnybara energikällor.

8. Acknowledgements

är för att jag har haft dig vid min sida. Vi har en spännande tid framför oss och får se var vi hamnar. Men i slutändan spelar det inte så stor roll eftersom vi får ta oss an äventyret tillsammans.

References

[1] Earth Science Communications Team at NASA's Jet Propulsion Laboratory. Vital signs. climate.nasa.gov/vital-signs/global-temperature/, accessed: Thur. 2 Feb 2023.

[2] IPCC, 2023: Climate Change 2023: Synthesis Report. A Report of the Intergovernmental Panel on Climate Change. Contribution of Working Groups I, II and III to the Sixth Assessment Report of the Intergovernmental Panel on Climate Change [Core Writing Team, H. Lee and J. Romero (eds.)]. IPCC, Geneva, Switzerland, (in press).

[3] Arrhenius S. On the Influence of Carbonic Acid in the Air upon the Temperature of the Ground. *Philosophical Magazine and Journal of Science*, 41:237–276, 1896.

[4] Paris IEA. CO_2 emissions in 2022, 2023. www.iea.org/reports/co2-emissions-in-2022, accessed 2023-11-17.

[5] Rosado P. Ritchie H., Roser M. CO_2 and greenhouse gas emissions. *Our World in Data*, 2020. https://ourworldindata.org/co2-and-greenhouse-gas-emissions, accessed 2023-11-17.

[6] Holechek, J.L.; Geli, H.M.E.; Sawalhah, M.N.; Valdez, R. A Global Assessment: Can Renewable Energy Replace Fossil Fuels by 2050? *Sustainability*, 14, 2022.

[7] Guo X., Liang C., Umar M., Mirza N. The impact of fossil fuel divestments and energy transitions on mutual funds performance. *Technological Forecasting and Social Change*, 176, 2022.

[8] Press release. NobelPrize.org. Nobel Prize Outreach AB 2023. https://www.nobelprize.org/prizes/chemistry/2019/press-release/, accessed: Mon. 23 Jan 2023.

[9] Xu K. Electrolytes and Interphases in Li-Ion Batteries and Beyond. *Chem. Rev.*, 114:11503–11618, 2014.

[10] Xu K. Nonaqueous Liquid Electrolytes for Lithium-Based Rechargeable Batteries. *Chem. Rev.*, 104:4304 – 4417, 2004.

[11] Melin T., Lundström R., Berg E.J. Revisiting the Ethylene Carbonate – Propylene Carbonate Mystery with Operando Characterization. *Adv. Mater. Interfaces*, 2101258, 2021.

[12] Xu K. Interfaces and interphases in batteries. *Journal of Power Sources*, 559:232652, 2023.

[13] Aurbach D., Zinigrad E., Cohen Y., Teller H. A short review of failure mechanisms of lithium metal and lithiated graphite anodes in liquid electrolyte solutions. *Solid State Ionics*, 148:405 – 416, 2002.

[14] Li C., Zhang H.P., Fu L.J, Liu H., Wu Y.P., Rahm E., Holze R., Wu H.Q. Cathode materials modified by surface coating for lithium ion batteries. *Electrochimica Acta*, 51:3872–3883, 2006.

[15] Birkl C. R., Roberts M. R., McTurk E., Bruce P. G., Howey D. A. Degradation diagnostics for lithium ion cells. *Journal of Power Sources*, 341:373–386, 2017.

[16] Menkin S., O'Keefe C.A., Gunnarsdóttir A.B., Dey S., Pesci F.M., Shen Z., Aguadero A., Grey C.P. Toward an Understanding of SEI Formation and Lithium Plating on Copper in Anode-Free Batteries. *J. Phys. Chem. C*, 125, 2021.

[17] Gao X., Zhou Y., Han D., Zhou J., Zhou D., Tang W., Goodenough J.B. Thermodynamic Understanding of Li-Dendrite Formation. *Joule*, 4, 2020.

[18] Peled E., Menkin S. Review—SEI: Past, Present and Future . *J. Electrochem. Soc.*, 164:A1703–A1719, 2017.

[19] Gao Y., Zhang B. Probing the Mechanically Stable Solid Electrolyte Interphase and the Implications in Design Strategies. *Adv. Mater.*, 35:2205421, 2023.

[20] Burns J. C., Sinha N. N., Coyle D. J., Jain G., VanElzen C. M., Lamanna W. M., Xiao A., Scott E., Gardner J. P., Dahn J. R. The Impact of Varying the Concentration of Vinylene Carbonate Electrolyte Additive in Wound Li-Ion Cells. *J. Electrochem. Soc.*, 159:A85–A90, 2011.

[21] Xiong D., Burns J. C. Smith A. J., Sinha N., Dahn J. R. A High Precision Study of the Effect of Vinylene Carbonate (VC) Additive in Li/Graphite Cells. *J. Electrochem. Soc.*, 158:A1431, 2011.

[22] Han B., Zhang Z., Zou Y., Xu K., Xu G., Wang H., Meng H., Deng Y.,Li J., Gu M. Poor Stability of Li_2CO_3 in the Solid Electrolyte Interphase of a Lithium-Metal Anode Revealed by Cryo-Electron Microscopy. *Adv.Mater.*, 33:2100404, 2012.

[23] Peled E. The Electrochemical Behavior of Alkali and Alkaline Earth Metals in Nonaqueous Battery Systems—The Solid Electrolyte Interphase Model. *Journal of The Electrochemical Society*, 126:2047–2051, 1979.

[24] Fong R., von Sacken U., Dahn J. R. Studies of Lithium Intercalation into Carbons Using Nonaqueous Electrochemical Cells . *Journal of The Electrochemical Society*, 137:2009–2013, 1990.

[25] Geronov Y., Schwager F., Muller R. H. Electrochemical Studies of the Film Formation on Lithium in Propylene Carbonate Solutions under Open-Circuit Conditions. *J. Electrochem. Soc*, 129:1422, 1982.

[26] Zaban A., Zinigrad E., Aurbach D. Impedance Spectroscopy of Li Electrodes. 4. A General Simple Model of the Li-SolutionInterphase in Polar Aprotic Systems. *J. Phys. Chem.*, 100:3089–3101, 1996.

[27] Peled E., Golodnitsky O., Ardel G. Advanced Model for Solid Electrolyte InterphaseElectrodes in Liquid and Polymer Electrolytes. *J.*

Electrochem. Soc., 144:L208–L210, 1997.

[28] Jagger B., Pasta M. Solid electrolyte interphases in lithium metal batteries. *Joule*, 7:2228–2244, 2023.

[29] Malmgren S., Ciosek K., Hahlin M., Gustafsson T., Gorgoi M., Rensmo H., Edström K. Comparing anode and cathode electrode/electrolyte interface composition and morphology using soft and hard X-ray photoelectron spectroscopy. *Electrochimica Acta*, 97:23–32, 2013.

[30] Aurbach D., Markovsky B.,Levi M.D.,Levi E., Schechter A., Moshkovich M.,Cohen Y. New insights into the interactions between electrode materials and electrolyte solutions for advanced nonaqueous batteries. *Journal of Power Sources*, 81-82:95–111, 1999.

[31] Edstrom K., Herstedt M., Abraham D. P. A new look at the solid electrolyte interphase on graphite anodes in Li-ion batteries . *Journal of Power Sources*, 153:380–384, 2006.

[32] Dollé M., Grugeon S., Dupont L., Tarascon J-M. In situ TEM study of the interface carbon/electrolyte. *Journal of Power Sources*, 97-98:104–106, 2001.

[33] Single F., Horstmann B.,Latz A. Revealing SEI Morphology: In-Depth Analysis of a Modeling Approach. *Journal of The Electrochemical Society*, 164:E3132–E3145, 2017.

[34] Lu P., Li C., Schneider E.W., Harris S.J. Chemistry, Impedance, and Morphology Evolution in Solid Electrolyte Interphase Films during Formation in Lithium Ion Batteries. *J. Phys. Chem. C*, 118:96–903, 2013.

[35] Huang W., Attia P.M., Wang H., Renfrew S.E., Jin N., Das S., Zhang Z., Boyle D. T., Li Y., Bazant M. Z., McCloskey B.D., Chueh W.C., Cui Y. Evolution of the Solid Electrolyte Interphase on Carbonaceous Anodes Visualized by Atomic-Resolution Cryogenic Electron Microscopy. *Nano Lett.*, 19:5140–4148, 2019.

[36] Lundström R., Gogoi N., Hou X., Berg E.J. Competing ethylene carbonate reactions on carbon electrode in Li-ion batteries. *Journal of The Electrochemical Society*, 170, 2023.

[37] Liu Y., Zhao C., Du J., Zhang X., Chen A., Zhang Q. Research Progresses of Liquid Electrolytes in Lithium-Ion Batteries. *Small*, 19:2205315, 2023.

[38] Forestier C., Grugeon S., Davoisne C., Lecocq A., Marlair G., Armand M., Sannier L., Laruelle S. Graphite electrode thermal behavior and solid electrolyte interphase investigations: Role of state-of-the-art binders, carbonate additives and lithium bis(fluorosulfonyl)imide salt. *Journal of Power Sources*, 330:186–194, 2016.

[39] Xu M., Tsiouvaras N., Garsuch A., Gasteiger H. A., Lucht B. L. Generation of Cathode Passivation Films via Oxidation of LithiumBis(oxalato) Borate on High Voltage Spinel ($LiNi_0 \cdot 5Mn_1 \cdot 5O_4$). *The Journal of Physical Chemistry C*, 118, 2014.

[40] Han J., Kim K., Lee Y., Choi N. Scavenging Materials to Stabilize

LiPF6-Containing Carbonate-Based Electrolytes for Li-Ion Batteries. *Adv. Mater.*, 31:1804822, 2019.

[41] Gogoi N., Bowall E., Lundström R., Mozhzhukhina N., Hernández G., Broqvist P., Berg E.J. Silyl-Functionalized Electrolyte Additives and Their Reactivity toward Lewis Bases in Li-Ion Cells. *Chem. Mater.*, 34:3831–3838, 2022.

[42] Mogi R., Inabac M., Iriyama Y., Abe T., Ogumi Z. Study on the decomposition mechanism of alkyl carbonate on lithium metal by pyrolysis-gas chromatography-mass spectroscopy. *Journal of Power Sources*, 121:597–603, 2003.

[43] Imhof R., Novák P. In situ investigation of the electrochemical reduction of carbonate electrolyte solutions at graphite electrodes. *J. Electrochem. Soc.*, 145:1081–1087, 1998.

[44] Novák P., Joho F., Imhof R., Panitz J.C., Haas O. In situ investigation of the interaction between graphite and electrolyte solutions. *Journal of Power Sources*, 1999.

[45] Onuki M., Kinoshita S., Sakata Y., Yanagidate M., Otake Y., Ue M., Deguchi M. Identification of the Source of Evolved Gas in Li-Ion Batteries Using ^{13}C-labeled Solvents. *Journal of The Electrochemical Society*, 155:A794–A797, 2008.

[46] Moshkovich M., Cojocaru M., Gottlieb H.E., Aurbach D. The study of the anodic stability of alkyl carbonate solutions by in situ FTIR spectroscopy, EQCM, NMR and MS. *Journal of Electroanalytical Chemistry*, 497, 2001.

[47] Metzger M., Strehle B., Solchenbach S., Gasteiger H. A. Origin of H_2 Evolution in LIBs: H_2O Reduction vs. Electrolyte Oxidation. *Journal of The Electrochemical Society*, 163:A798–A809, 2016.

[48] Roland Jung R., Metzger M., Maglia F., Stinner C., Gasteiger H.A. Chemical versus Electrochemical Electrolyte Oxidation on NMC111, NMC622, NMC811, LNMO, and Conductive Carbon. *J. Phys. Chem. Lett.*, 8, 2017.

[49] Rinkel B.L.D., Hall D.S., Temprano I., Grey C.P. Electrolyte Oxidation Pathways in Lithium-Ion Batteries. *J. Am. Chem. Soc.*, 142, 2020.

[50] Metzger M., Strehle B., Solchenbach S., Gasteiger H. A. Hydrolysis of Ethylene Carbonate with Water and Hydroxide under Battery Operating Conditions. *Journal of The Electrochemical Society*, 163:1219–1225, 2016.

[51] Yoshida H., Fukunaga T., Hazama T., Terasaki M., Mizutani M., Yamachi M. . Degradation mechanism of alkyl carbonate solvents used in lithium-ion cells during initial charging. *Journal of Power Sources*, 68:311–315, 1997.

[52] Shin J., Chi-Hwan Han C., Jung U., Leeb S., Kim H., Kim K. Effect of Li_2CO_3 additive on gas generation in lithium-ion batteries . *Journal of Power Sources*, 109:47–52, 2002.

[53] Seo D. M., Chalasani D., Parimalam B. S., Kadam R., Nie M., Lucht B. L. Reduction reactions of carbonate solvents for lithium ion batteries . *ECS Electrochemistry Letters*, 3:91–94, 2014.

[54] Schwenke K. U., Solchenbach S., Demeaux J., Lucht B. L., Gasteiger H. A. The Impact of CO_2 Evolved from VC and FEC during Formation of Graphite Anodes in Lithium-Ion Batteries . *Journal of The Electrochemical Society*, 166:A2035–A2047, 2019.

[55] Joho F., Novák P. SNIFTIRS investigation of the oxidative decomposition of organic-carbonate-based electrolytes for lithium-ion cells. *Electrochimica Acta*, 45:3589–3599, 2000.

[56] Aurbach D., Daroux M. L., Faguy P. W., Yeager E. Identification of Surface Films Formed on Lithium in Propylene Carbonate Solutions Identification of Surface Films Formed on Lithium in Propylene Carbonate Solutions. *Journal of The Electrochemical Society*, 134:1611, 1987.

[57] Leggesse E. G., Lin R. T., Teng T., Chen C., Jiang J. Oxidative Decomposition of Propylene Carbonate in Lithium IonBatteries: A DFT Study. *Electrochimica Acta*, 117:7959–7969, 2013.

[58] Lundström R., Gogoi N., Melin T., Berg E.J. Three Vinylene Carbonate Aspects Contributing to the Solid Electrolyte Interphase During Initial Formation Cycle in Li-Ion Batteries. *Manuscript*, 2023.

[59] Pritzl D., Solchenbach S., Wetjen M., A. Gasteiger H.A. Analysis of Vinylene Carbonate (VC) as Additive in Graphite/LiNi$_{0.5}$Mn$_{1.5}$O$_4$ Cells. *Journal of The Electrochemical Society*, 164:A2625–A2635, 2017.

[60] Metzger M., Walke P., Solchenbach S., Salitra G., Aurbach D., Gasteiger H.A. Evaluating the High-Voltage Stability of Conductive Carbon and Ethylene Carbonate with Various Lithium Salts. *Journal of The Electrochemical Society*, 167, 2020.

[61] Guéguen A., Streich D., He M., Mendez M., Chesneau F. F., Novák P., Berg E. J. Decomposition of LiPF$_6$ in High Energy Lithium-Ion Batteries Studied with Online Electrochemical Mass Spectrometry . *Journal of The Electrochemical Society*, 163:A1095–A1100, 2016.

[62] Campion C. L., Li W., Lucht B. L. Thermal Decomposition of LiPF$_6$-Based Electrolytes for Lithium-Ion Batteries. *Journal of The Electrochemical Society*, 152:A2327–A2334, 2005.

[63] Yang H., Zhuang G.V., Ross P.N. Jr. Thermal stability of LiPF$_6$ salt and Li-ion battery electrolytes containing LiPF$_6$. *Journal of Power Sources*, 161, 2006.

[64] Gachot G., Ribière P.,Mathiron D., Grugeon S., Armand M., Leriche J.-B., Pilard S., Laruelle S. Gas Chromatography/Mass Spectrometry As a Suitable Tool for the Li-Ion Battery Electrolyte Degradation Mechanisms Study. *Anal. Chem.*, 83, 2011.

[65] Lundström R., Melin T., King L., Berg E.J. LiBOB SEI. Thickness,

composition, reaction pathways on carbon electrode. *Manuscript*, 2023.

[66] Metzger M., Marino C., Sicklinger J., Haering D., Gasteiger H.A. In situ investigation of the interaction between graphite and electrolyte solutions. *J. Electrochem. Soc.*, 162, 2015.

[67] Kitz P.G., Lacey M.J., Novák P., Berg E.J. Operando EQCM-D with Simultaneous in Situ EIS: New Insights intoInterphase Formation in Li Ion Batteries. *Anal. Chem.*, 91, 2019.

[68] Keith A. Nier, Alfred L. Yergey, and P. Jane Gale. A general chronicle of mass spectrometry and guide to the scope of the volume. In *The Encyclopedia of Mass Spectrometry*. Elsevier, Boston, 2016.

[69] Dawson P. H. *Quadrpole mass spectrometry*. Elsevier Scientific Publishing Company, 1976.

[70] Schlüter N., Novák P., Schröder D. Nonlinear Electrochemical Analysis: Worth the Effort to Reveal New Insights into Energy Materials. *Adv. Energy Mater*, 12:2200708, 2022.

[71] Kim S., Kim H., Kim B., Kim Y., Jung J., Ryu W. In Situ Gas Analysis by Differential Electrochemical MassSpectrometry for Advanced Rechargeable Batteries: A Review. *Adv. Energy Mater.*, 13:2301983, 2023.

[72] Rowden B., Garcia-Araez N. A review of gas evolution in lithium ion batteries. *Energy Reports*, 6:10–18, 2020.

[73] Li H., Guo S., Zhou H. In-situ/operando characterization techniques in lithium-ion batteries and beyond. *Journal of Energy Chemistry*, 59:191–211, 2021.

[74] Wolter O., Heitbaum J. Differential electrochemical mass spectroscopy (DEMS) - a new method for the study of electrode processes. *Berichte der Bunsengesellschaft für Phys. Chemie*, 6:2–6, 1984.

[75] Novák P., Goers D., Hardwick L., Holzapfel M., Scheifele W., Ufheil J., Würsig A. Advanced in situ characterization methods applied to carbonaceous materials. *Journal of Power Sources*, 146:15–20, 2005.

[76] McCloskey B. D., Bethune D. S., Shelby R. M., Girishkumar G., Luntz, A. C. Solvents critical role in nonaqueous Lithium-Oxygen battery electrochemistry. *Journal of Physical Chemistry Letters*, 2:1161–1166, 2011.

[77] Berg E. J., Novák P. PSI Electrochemistry Laboratory - Annual Report. *Annual Report 2012*, page 47, 2012.

[78] Tsiouvaras N., Meini S., Buchberger I., Gasteiger H. A. A Novel On-Line Mass Spectrometer Design for the Study of Multiple Charging Cycles of a $Li-O_2$ Battery. *Journal of The Electrochemical Society*, 160:A471–A477, 2013.

[79] He M. *Elucidating interface reactions in Li-ion batteries and supercapacitors by in situ gas analysis*. PhD thesis, ETH Zurich, 2016.

[80] Misiewicz C. *Exploring Ageing Mechanisms in Li-ion Batteries via Online Electrochemical Mass Spectrometry*. Licentiate thesis. Uppsala

University. 2023.

[81] Lundström R., Gogoi N., Hou X., Berg E.J. Design and validation of an online partial and total pressure measurement system for Li-ion cells. *Journal of Power Sources*, 405, 2021.

[82] Bernhard R., Metzger M., Gasteiger H. A. Gas Evolution at Graphite Anodes Depending on Electrolyte Water Content and SEI Quality Studied by On-Line Electrochemical Mass Spectrometry. *Journal of The Electrochemical Society*, 162:1984–1989, 2015.

[83] Sauerbrey, G. Verwendung von Schwingquarzen zur Wägung dünner Schichten und zur Mikrowägung. *Z. Physik*, 155:206–222, 1959.

[84] Johannsmann D. *The Quartz Crystal Microbalance in Soft Matter Research*. Springer Cham, 2015.

[85] Reviakine I., Johannsmann D., Richter R. P. Hearing What You Cannot See and Visualizing What You Hear: Interpreting Quartz Crystal Microbalance Data from Solvated Interfaces. *Anal. Chem.*, 83:8838–8848, 2011.

[86] Solchenbach S., Metzger M., Egawa M., Beyer H., Gasteiger H. A. Quantification of PF_5 and POF_3 from Side Reactions of $LiPF_6$ in Li-Ion Batteries. *Journal of The Electrochemical Society*, 165:A3022, 2018.

[87] Barlow C. G. . Reaction of Water with Hexafluorophosphates and with Li Bis(perfluoroethylsulfonyl)imide Salt. *Electrochemical and Solid-State Letters*, 2:362–364, 1999.

[88] Henschel J., Peschel C., Klein S., Horsthemke F., Winter M., Nowak S. Clarification of Decomposition Pathways in a State-of-the-Art Lithium Ion Battery Electrolyte through 13C-Labeling of Electrolyte Components. *Angewandte Chemie*, 132:6184–6193, 2020.

[89] Spotte-Smith E. W. C., Kam R. L., Barter D., Xie X., Hou T., Dwaraknath S., Blau S. M., Persson K. A. Toward a Mechanistic Model of Solid Electrolyte Interphase Formation and Evolution in Lithium Ion Batteries. *ACS Energy Lett.*, 7:1446–1453, 2022.

[90] Fergus J. W. Recent developments in cathode materials for lithium ion batteries. *Journal of Power Sources*, 195:939–954, 2010.

[91] Tesfamhret Y., Younesi R., Berg E. J. Influence of Al_2O_3 Coatings on HF Induced Transition Metal Dissolution from Lithium-Ion Cathodes. *Journal of The Electrochemical Society*, 169:010530, 2022.

[92] Chen Z., Lu Z., Dahn J. R. Staging Phase Transitions in Li_xCoO_2. *Journal of The Electrochemical Society*, 149:A1604, 2002.

[93] Kikkawa J., Terada S., Gunji A., Nagai T., Kurashima K., Kimoto K. Chemical states of overcharged $LiCoO_2$ particle surfaces and interiors observed using electron energy-loss spectroscopy. *Journal of Physical Chemistry C*, 119:15823–15830, 2015.

[94] Wang H., Rus E., Sakuraba T., Kikuchi J., Kiya Y., Abruna H.D. CO_2 and O_2 evolution at high voltage cathode materials of li-ion batteries: A differential electrochemical mass spectrometry study. *Analytical Chem-*

istry, 86:6197–6201, 2014.

[95] House R. A. Rees G. J., Pérez-Osorio M. A., Marie J., Boivin E., Robertson A. W., Nag A., Garcia-Fernandez M., Zhou K., Bruce P. G. First-cycle voltage hysteresis in Li-rich 3d cathodes associated with molecular O_2 trapped in the bulk. *Nature Energy*, 5:777–785, 2020.

[96] Wandt J., Freiberg A. T. S., Ogrodnik A., Gasteiger H. A. Singlet oxygen evolution from layered transition metal oxide cathode materials and its implications for lithium-ion batteries. *Materials Today*, 21:825–833, 2018.

[97] Xu K. Whether EC and PC Differ in Interphasial Chemistry on Graphitic Anode and How. *Journal of The Electrochemical Society*, 156:A751, 2009.

[98] Zhuang G. V., Yang H., Blizanac B., Ross Jr P. N. A Study of Electrochemical Reduction of Ethylene and Propylene Carbonate Electrolytes on Graphite Using ATR-FTIR Spectroscopy. *Electrochem. Solid-State Lett.*, 8:A441, 2005.

[99] Zhang H., Sun C., Li F., Liu C., Tan J., Cheng H. New Insight into the Interaction between Propylene Carbonate-Based Electrolytes and Graphite Anode Material for Lithium Ion Batteries. *J. Phys. Chem. C*, 12:4740–4748, 2007.

[100] Zhuang G. V., Xu K., Yang H., Jow T. R., Ross P. N. Lithium ethylene dicarbonate identified as the primary product of chemical and electrochemical reduction of EC in 1.2 M $LiPF_6$/EC:EMC electrolyte. *Journal of Physical Chemistry B*, 109:17567–17573, 2005.

[101] Nagaoka T., Fukunaga T., Yoshino T., Watanabe I., Nakayama T., Okazaki S. Uptake of Ions into Electrochemically Treated Glassy Carbon. *Anal. Chem.*, 60:2766–2769, 1988.

[102] Spahr M. E., Wilhelm H., Palladino T., Dupont-Pavlovsky N., Goers D., Joho F., Novák P. The role of graphite surface group chemistry on graphite exfoliation during electrochemical lithium insertion. *Journal of Power Sources*, 119-121:543–549, 2003.

[103] Spahr M. E., Buqa H., Würsig A., Goers D., Hardwick L., Novák P., Krumeich F., Dentzer J., Vix-Guterl C. Surface reactivity of graphite materials and their surface passivation during the first electrochemical lithium insertion. *Journal of Power Sources*, 153:300–311, 2006.

[104] Strmcnik D., Castelli I. E., Connell J. G., Haering D., Zorko M., Martins P., Lopes P. P., Genorio B., Østergaard T., Gasteiger H. A., Maglia F., Antonopoulos B. K., Stamenkovic V. R., Rossmeisl J., Markovic N. M. Electrocatalytic transformation of HF impurity to H2 and LiF in lithium-ion batteries. *Nature Catalysis*, 1:255–262, 2018.

[105] Parimalam B. S., MacIntosh A. D., Kadam R., Lucht B. L. Decomposition Reactions of Anode Solid Electrolyte Interphase (SEI) Components with $LiPF_6$. *J. Phys. Chem. C*, 121:22733–22738, 2017.

[106] Ota H., Sakata Y., Inoue A., Yamaguchi S. Analysis of Vinylene Car-

bonate Derived SEI Layers on Graphite Anode. *J. Electrochem. Soc.*, 151:A1659, 2004.

[107] Buqa H., Würsig A., Vetter J., Spahr M. E., Krumeich F., Novák P. SEI Film Formation on Highly Crystalline Graphitic Materials in Lithium-Ion Batteries. *Journal of Power Sources*, 153:285–390, 2006.

[108] Pieczonka N. P. W., Yang L., Balogh M. P., Powell B. R., Chemelewski K., Manthiram A., Krachkovskiy S. A., Goward G. R., Liu M., Kim J. H. Impact of Lithium Bis(Oxalate)Borate Electrolyte Additive on the Performance of High-Voltage Spinel/Graphite Li-Ion Batteries. *J. Phys. Chem. C*, 117:22603–22612, 2012.

[109] Li J., Yang J., Ji Z., Su M., Li H., Wu Y., Su X. Prospective Application, Mechanism, and Deficiency of Lithium Bis(Oxalate)Borate as the Electrolyte Additive for Lithium-Batteries. *Adv. Energy Mater.*, 13:2301422, 2023.

[110] Kubot M., Balke L., Scholz J., Wiemers-Meyer S., Karst U., Hayen H., Hur H., Winter M., Kasnatscheew J., Nowak S. High-Voltage Instability of Vinylene Carbonate (VC): Impact of Formed Poly-VC on Interphases and Toxicity. *Adv. Sci.*, 11:2305282, 2024.

Acta Universitatis Upsaliensis

Digital Comprehensive Summaries of Uppsala Dissertations from the Faculty of Science and Technology 2363

Editor: The Dean of the Faculty of Science and Technology